(Supplementary Table S2)[33], and found that 18 exons are similarly regulated by *Mbnl1* knockdown in undifferentiated C2C12 cells (Supplementary Fig. S6d and Table S2).

We combined datasets C and M into a single composite pre-mRNA and made integrated RNA maps from our HITS-CLIP reads mapped to the corresponding genomic regions as previously described for Nova[30] and PTB[36]. This showed that CUGBP1 binding to upstream intronic regions facilitates exon skipping, whereas CUGBP1 binding to downstream intronic regions promotes exon inclusion (closed arrows in Fig. 2b and Supplementary Fig. S7a). Results of the 2nd experiments are shown in Fig. 2 and those of the 1st experiments are in Supplementary Fig. S7. In contrast, although the binding sites of MBNL1 are more diffusely distributed and less abundant in regions flanking splice sites (Fig. 2c), MBNL1 binding close to the 3′ end of the downstream intron induces exon skipping (closed arrow in Fig. 2c and Supplementary Fig. S7b). The presence of a similar peak in dataset M2 (closed arrow in Supplementary Fig. S7c) further supports this observation.

We next analyzed the interaction between CUGBP1 and MBNL1 in splicing regulation. We made an RNA map of CUGBP1-binding sites in MBNL1-regulated exons from datasets M and M2 (Fig. 2d and Supplementary Fig. S7e), as well as an RNA map of MBNL1-binding sites in CUGBP1-regulated exons from dataset C (Fig. 2e and Supplementary Fig. S7f). Both RNA maps demonstrate the presence of CUGBP1 clusters in MBNL1-responsive exons and vice versa, which suggests that CUGBP1 and MBNL1 are likely to regulate alternative splicing of some of the same exons.

MBNL1 and CUGBP1 both preferentially bind to the 3′ UTR. MBNL1 has so far solely been categorized as an exon/intron-binding splicing regulatory protein[6], but to our surprise we found that the majority (55%) of MBNL1-binding regions are located in 3′ UTRs (Fig. 3a). The same pattern with preferential binding (53%) in 3′ UTRs is observed for CUGBP1, while only 2% of PTB binding regions are located in 3′ UTRs (Fig. 3a). Similarly, when HITS-CLIP tags are mapped to the size-normalized positions of all the genes in the mouse genome, CUGBP1 and MBNL1 CLIP tags, but not PTB CLIP-tags, are enriched close to the 3′ ends of genes (Fig. 3b). Additionally, 610 3′ UTRs, which constitutes 28.7% of the CUGBP1-tagged 3′ UTRs and 17.4% of the MBNL1-tagged 3′ UTRs, are shared

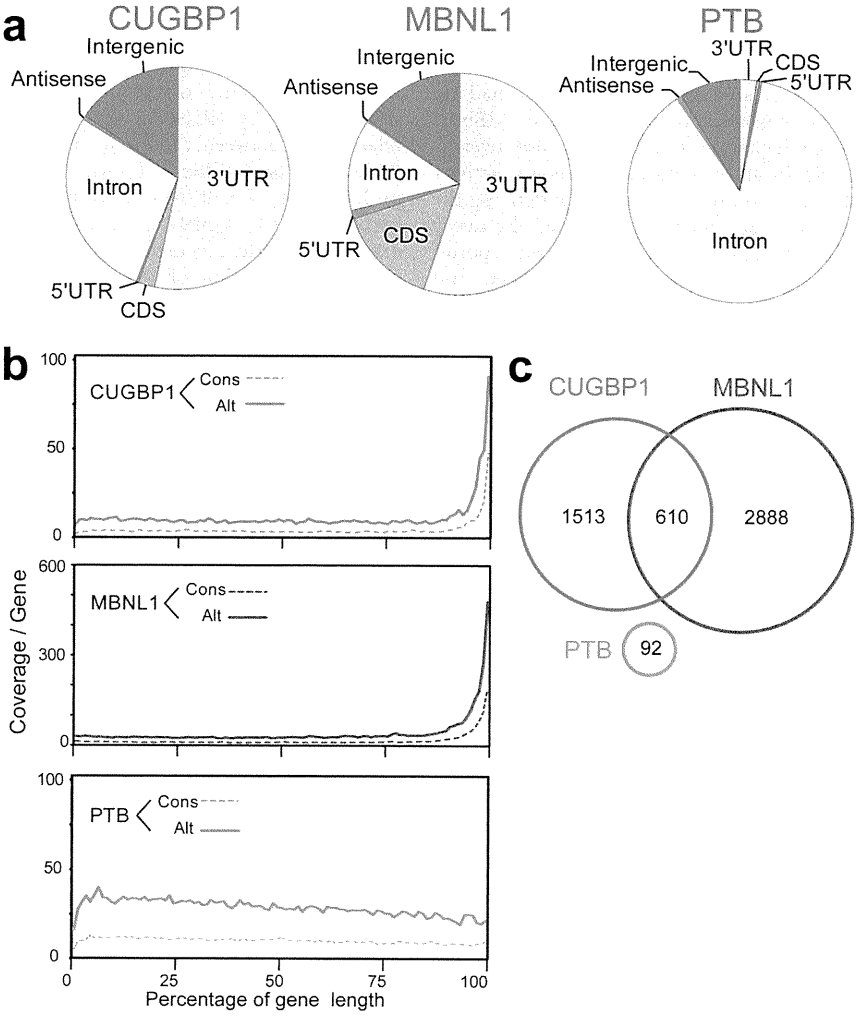

Figure 3 | Enrichment of CUGBP1 and MBNL1 CLIP-tags in the 3′ UTR. (a) Distributions of CUGBP1, MBNL1, and PTB binding regions. Binding regions are mapped to CDS (coding sequence), 5′ and 3′ UTRs, introns, intergenic regions (incl. tRNA and rRNA genes), or antisense within genes according to the UCSC knownGene annotation of the NCBI Build 37.1 mouse genome (mm9). Pie-charts show ratios of binding regions mapped to the indicated regions. (b) Distributions of CUGBP1, MBNL1, and PTB CLIP-tags mapped to the relative positions of all the mouse genes. The relative positions of the genes are shown in percentages of the gene length in abscissa. The broken lines represent 15,638 genes with constitutive transcriptional start and end sites (Cons), and the solid lines represent 7,477 genes with alternative transcriptional start or end site (Alt). (c) Venn diagram of the numbers of genes with CUGBP1-, MBNL1-, and PTB-binding regions within the 3′ UTR. Binding regions were identified using the SeqMonk software.

between these two proteins (Fig. 3c). All these data document that both CUGBP1 and MBNL1 preferentially bind to 3′ UTRs, indicating that this is a key function of both proteins in RNA processing. This suggests that the functional repertoire of MBNL1 should be expanded and that MBNL1, from being primarily regarded as regulator of alternative splicing, should also be considered as an important regulator of 3′ UTR-mediated processes, such as mRNA stability/degradation.

MBNL1 destabilize mRNAs. To analyze the function of CUGBP1/MBNL1 binding to 3′ UTRs, we made luciferase reporter constructs harboring CUGBP1/MBNL1-binding sites in the 3′ UTR. Since no CLIP tags were observed in the 3′ UTR of *Gapdh* (Supplementary Fig. S8), we made a *luciferase-Gapdh* 3′ UTR expression vector, and then inserted 12 repeats of GT and 7 repeats of CTG immediately after the stop codon of *luciferase* to introduce a CUGBP1-binding site (GU rich motif) and an MBNL1-binding site (YGCY motif), respectively (Fig. 4a). We also inserted 12 AC repeats as a control. Due to the high expression level of CUGBP1 in C2C12 cells we used HEK293 cells for transient transfection of these reporter constructs along with CUGBP1/MBNL1 expression vectors. For the constructs with *Gapdh* 3′ UTR alone or with AC repeats inserted, overexpression of CUGBP1 or MBNL1 had no effect on luciferase activity (Fig. 4b). For the GT repeat construct, overexpression of CUGBP1 decreased the luciferase activity, but MBNL1 had no effect. For the CTG repeat construct overexpression of MBNL1 dramatically decreased the luciferase activity, and also overexpression of CUGBP1 significantly reduced luciferase activity (Fig. 4b). In order to shed light on the mechanism underlying the observed decrease in luciferase activity we investigated the decay of *luciferase* mRNA. The SV40 promoter of the luciferase reporter constructs was replaced with a tet-repressible promoter, and HEK293 Tet-off cells were transiently transfected with these constructs. Doxycycline was added to the medium to stop transcription of the tet-responsive promoter, and the temporal profiles of *luciferase* and *GAPDH* mRNA levels were measured. Overexpression of MBNL1 together with the CTG repeat reporter construct resulted in highly increased decay of *luciferase* mRNA and CUGBP1 overexpression together with the GT repeat reporter construct also increased mRNA decay. Overexpression of either protein together with the *Gapdh* 3′ UTR control construct did not alter mRNA decay (Fig. 4c). These data demonstrate that binding of CUGBP1 and MBNL1 to the 3′ UTR promotes mRNA decay. To examine whether CUGBP1 and MBNL1 regulate decay of endogenous mRNAs, we next analyzed mRNA stability in actinomycin D treated C2C12 cells by expression arrays following siRNA knock down of CUGBP1 or MBNL1 (GEO accession number, GSE27583). To identify genes with reliable half-life estimates, we restricted our analysis to 195 transcripts using three conditions: (i) half-life between 2.5–5 hrs; (ii) correlation coefficient of fitting to an exponential decay greater than 0.9; and (iii) RMA-normalized signal values more than 100 at all time points. The median half-life of all the transcripts matching these criteria in the control is 3.56 hrs, whereas those from CUGBP1- and MBNL1-knocked down cells are significantly prolonged to 3.91 hrs and 3.73 hrs, respectively (Fig. 5a). We chose four additional representative mRNAs with a cluster of either CUGBP1- or MBNL1-tags in the 3′UTR, and confirmed by real time PCR that knockdown of either CUGBP1 or MBNL1 results in approximately two-fold increase in mRNA half-life of these target mRNAs (Fig. 5b). The half-lives of 100 out of 195 transcripts are prolonged both by knockdown of CUGBP1 and MBNL1, suggesting overlapping activity in the regulation of mRNA decay by CUGBP1 and MBNL1. We next analyzed the relationship between change in mRNA half-life and coverage of HITS-CLIP tags in the 3′ UTRs. We found that genes displaying prolongation of half-lives in response to CUGBP1 knockdown harbors more CUGBP1-tags in their 3′ UTRs, compared to those displaying shortening of half-lives (Fig. 5c). Similarly, genes that display prolongation of their half-lives in response to MBNL1 knockdown have more MBNL1-tags in their 3′ UTRs (Fig. 5c).

Gene Ontology analysis of CUGBP1/MBNL1-bound 3′ UTRs revealed that the terms 'cytoskeletal protein binding, 'transcription factor binding' and 'RNA binding' are significantly overrepresented for CUGBP1- and MBNL1-bound genes (Table 1).

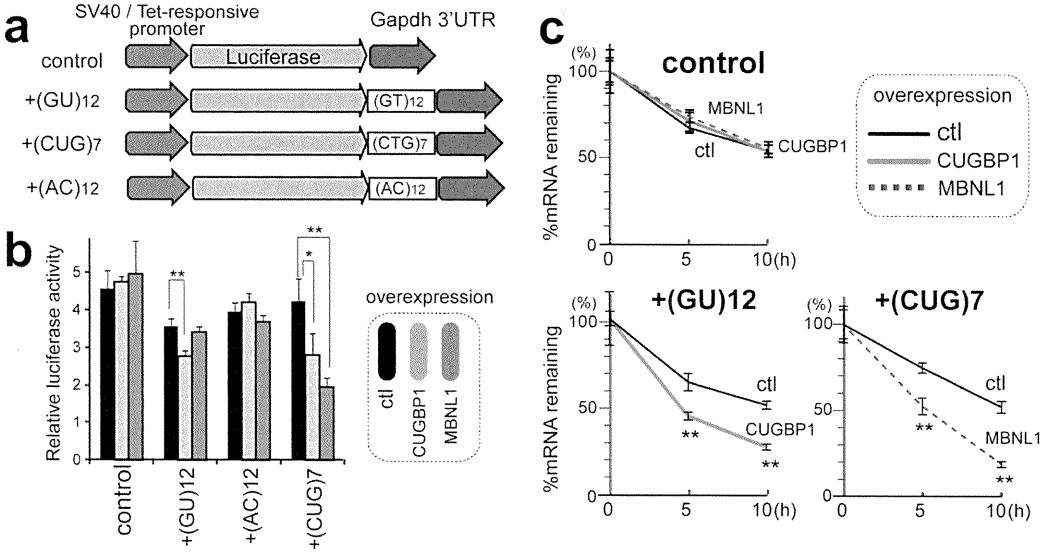

Figure 4 | Decay of *luciferase* mRNA by overexpression of CUGBP1/MBNL1. (a) Schemes of luciferase reporter plasmids harboring Gapdh 3′ UTR. Each construct was made carrying either SV40 or tet-responsive promoter. (b) Luciferase activity after overexpression of CUGBP1/MBNL1. HEK293 cells were transfected with the indicated SV40-driven luciferase reporter constructs. Luciferase activity is normalized for the transfection efficiency using co-transfection of pRL/SV40. (c) Decay of luciferase mRNA after overexpression of CUGBP1/MBNL1. HEK293 Tet-off cells were transfected with the indicated tet-responsive promoter-driven luciferase reporter constructs. Doxycycline was added to the medium to stop transcription at time 0. Temporal profiles of luciferase mRNA decay were quantified by real time RT-PCR and are normalized for Gapdh mRNA levels. All experiments were triplicated, and the mean and s.d. are indicated (* $p < 0.05$; ** $p < 0.01$).

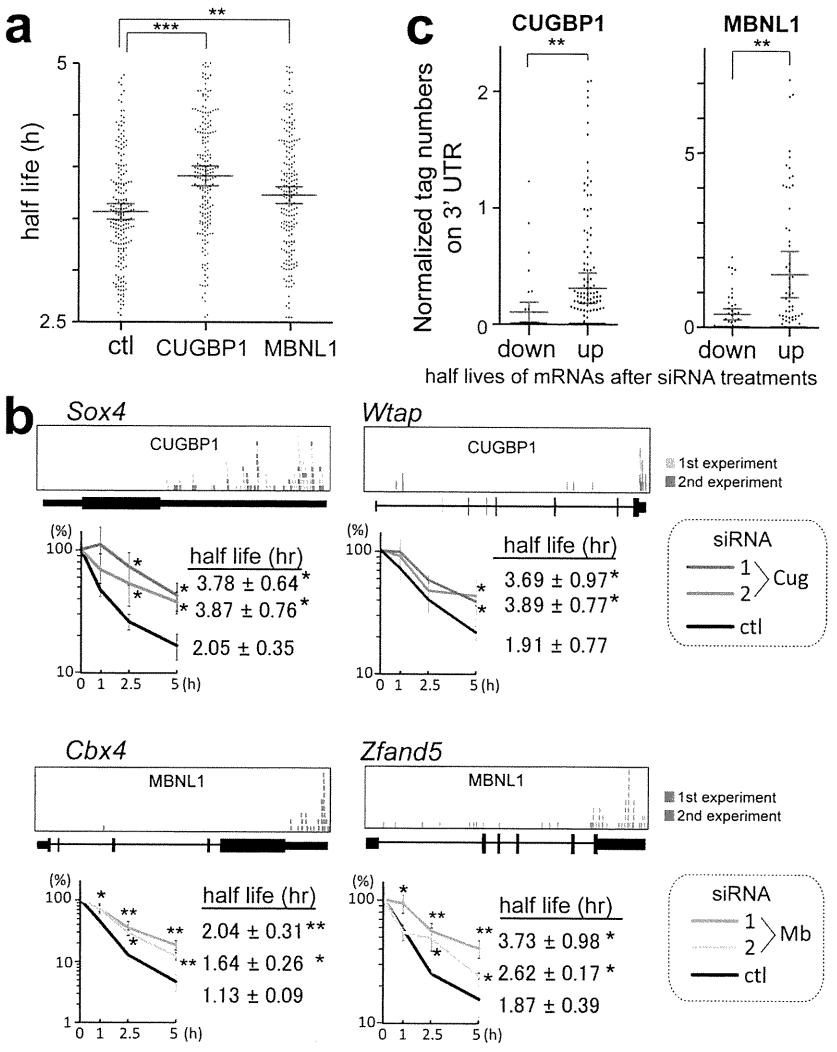

Figure 5 | Global analysis of mRNA decay by expression array of C2C12 cells treated with CUGBP1/MBNL1 siRNA. (a) Half-lives of mRNAs in C2C12 cells with the indicated siRNAs. Red lines represent means and 95% confidence intervals. ** $p < 0.01$ and *** $p < 0.001$. (b) Real-time RT-PCR analysis of the stability of four representative endogenous mRNAs, which were detected by expression arrays. CLIP-tag distributions are shown above each gene structure. C2C12 cells were treated with either control (ctl), CUGBP1 (Cug), or MBNL1 (Mb) siRNA. Actinomycin D was added to the medium to stop transcription at time 0. Temporal profiles of decay of the indicated genes were analyzed by real-time RT-PCR and are normalized for Gapdh mRNA levels. All experiments were triplicated, and the mean and s.d. are indicated (* $p < 0.05$ and ** $p < 0.01$). (c) Tag counts in the 3′ UTR of each gene are plotted in two categories of prolonging (up) and shortening (down) of half-lives after MBNL1 and CUGBP1 siRNAs. Red lines represent means and 95% confidence intervals. ** $p < 0.01$. Tag counts were normalized by the gene expression level at 0 h of cells treated with control siRNA.

Table 1 | The five most frequent Gene Ontology terms of mRNAs that are bound by CUGBP1 and MBNL1 to the 3′ UTR

CLIP data	GO ID	Term	P Value
CUGBP1	GO:0008092	cytoskeletal protein binding	1.58E-06
	GO:0003723	RNA binding	1.40E-04
	GO:0008134	transcription factor binding	9.65E-04
	GO:0051082	unfolded protein binding	0.003184
	GO:0019904	protein domain specific binding	0.006603
MBNL1	GO:0008092	cytoskeletal protein binding	7.31E-20
	GO:0008134	transcription factor binding	2.20E-08
	GO:0003723	RNA binding	0.001893
	GO:0019899	enzyme binding	0.002046
	GO:0032553	ribonucleotide binding	0.004210

We utilized the mRNAs that have more than 8-fold coverage of CLIP tags in their 3′UTR for the analysis by DAVID[53,54].

PITX2 is a homeobox transcription factor that regulates left-right asymmetric morphogenesis[37,38] and it is also deeply implicated in myogenesis during mouse embryonic development[39–41]. We found that the decay of *Pitx2* mRNA is prolonged by knocking down MBNL1, but not CUGBP1 in undifferentiated C2C12 cells (Fig. 6b and c). This is consistent with the fact that *Pitx2* harbors a much higher number of MBNL1-CLIP tags than that of CUGBP1-CLIP tags in the 3′ UTR (Fig. 6a). We also observed that down regulation of both CUGBP1 and MBNL1 decreases the decay of *Myod1* and *Mbnl2* mRNA, but not that of *Gapdh* mRNA (Supplementary Fig. S8). Similarly, down regulation of CUGBP1 decreases the decay of other myogenic transcription factors such as *Myog* and *Mef2a* mRNAs, and also of *Cugbp2* (Supplementary Fig. S9). Furthermore, knockdown of CUGBP1 and MBNL1 prolongs decay of *Mbnl1* and *Cugbp1* mRNAs, respectively, suggesting a mechanism for cross-regulation of expression of MBNL1, CUGBP1, and their family proteins (Supplementary Fig. S8).

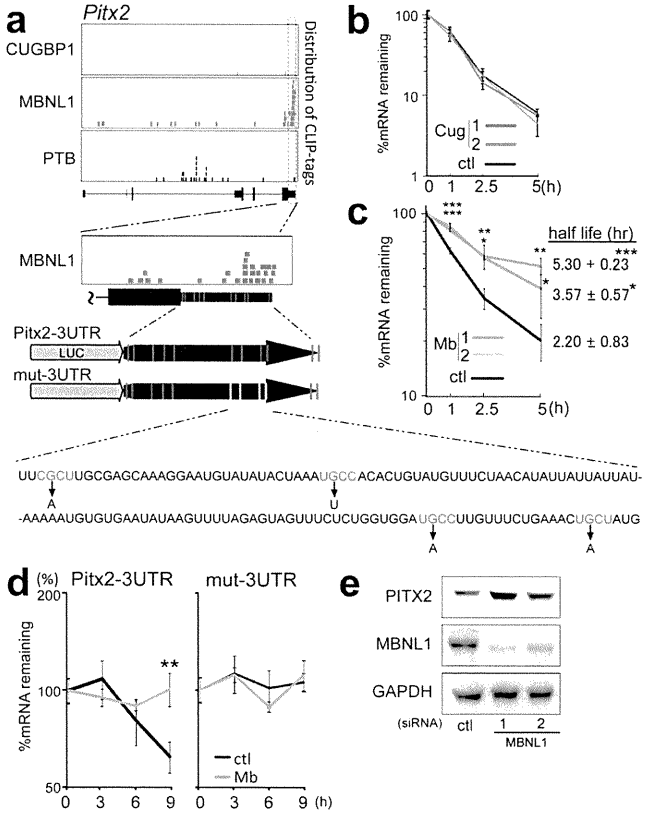

Figure 6 | MBNL1 binds to 3′ UTR of *Pitx2* and facilitates decay of *Pitx2* mRNA. (a) Distributions of MBNL1 CLIP-tags in the Pitx2-gene structure, and schemes of luciferase reporter plasmids harboring wild-type (Pitx2-3UTR) and mutated (mut-3UTR) 3′ UTRs of Pitx2. Red bars indicate locations of native YGCY motifs and yellow bars indicate those of mutated YGCY motifs. Individual mutations disrupting YGCY motifs are shown at the bottom. We introduced U at the 2nd YGCY motif to prevent formation of AU and AC repeats, which constitute a potential binding site of Hu proteins and hnRNP L, respectively. (b and c) Decay of endogenous Pitx2 mRNA by siRNA-mediated knockdown of CUGBP1 (b) and MBNL1 (c). C2C12 cells were treated with either control (ctl), CUGBP1 (Cug) or MBNL1 (Mb) siRNA. Actinomycin D was added to the medium to stop transcription at time 0. Temporal profiles of decay of the indicated genes were analyzed by real-time RT-PCR and were normalized for Gapdh mRNA levels. All experiments were triplicated, and the mean and s.d. are indicated (* $p < 0.05$; ** $p < 0.01$; *** $p < 0.001$). (d) Decay of luciferase mRNA in the Pitx2-3UTR and mut-3UTR constructs after either control (ctl) or MBNL1 (Mb) siRNA in TetON-C2C12 cells. Culture medium was replaced by medium without doxycycline to stop transcription at time 0. Temporal profiles of luciferase mRNA decay are quantified by real-time RT-PCR and are normalized for Gapdh mRNA levels. All experiments were triplicated, and the mean and s.d. are indicated (** $p < 0.01$). (e) Immunoblot of PITX2 in undifferentiated C2C12 cells at 48 hrs after transfection of MBNL1 siRNA.

To analyze more directly the role of MBNL1 binding to the 3′ UTR in regulation of mRNA decay, we examined the mRNA stability of firefly luciferase fused with the 3′ UTR of *Pitx2* (Fig. 6a). There are 11 YGCY motifs in the 3′ UTR of *Pitx2*, and 4 of the 11 motifs have MBNL1-CLIP tags. We introduced artificial mutations in these 4 motifs to prevent binding of MBNL1 (Fig. 6a). Consistent with the proposed role for MBNL1 in mRNA decay, we observe that disruption of the MBNL1-binding motifs in the *Pitx2*-3′ UTR abolished responsiveness to MBNL1 knockdown (Fig. 6d). Furthermore, immunoblots demonstrated that MBNL1-knockdown enhanced expression of endogenous PITX2 in C2C12 cells (Fig. 6e). These data suggest that MBNL1 promotes decay of *Pitx2* mRNA and thereby represses expression of the PITX2 protein.

Taken together, all of our data are consistent with a model where CUGBP1 and MBNL1 facilitate mRNA decay through binding to the 3′ UTR of target genes.

Discussion

CUGBP1 and MBNL1 are developmentally regulated RNA-binding proteins that are causally associated with myotonic dystrophy type 1. In this study, we show that both CUGBP1 and MBNL1 preferentially bind to 3′ UTRs and destabilize the bound mRNAs. In particular, we show that CUGBP1 and MBNL1 destabilize myogenic differentiation factors and RNA-binding proteins. In addition, our results confirm and significantly expand the current knowledge of the splicing-regulatory effects of CUGBP1 and MBNL1. Taken together, the data from the present study indicates that CUGBP1 and MBNL1 are closely related and cross regulate alternative splicing and mRNA decay.

MBNL1 binding to 3′ UTRs has not been previously reported. We show for the first time that MBNL1 binds to 3′ UTRs and promotes mRNA decay in both artificial constructs and in endogenous genes. We also demonstrate by expression arrays that both CUGBP1 and MBNL1 facilitate mRNA decay by binding to 3′ UTRs. The present study demonstrates global *in vivo* interactions between CUGBP1 and 3′ UTRs and reveals that CUGBP1 also preferentially binds to 3′ UTR rather than exons/introns. We provide *in vivo* evidence that CUGBP1 facilitates mRNA decay of a broad spectrum of genes in addition to the previously reported genes[25–27,42–44].

Interestingly, we find that MBNL1 promotes decay of *Cugbp1* mRNA and that CUGBP1 promotes decay of *Mbnl1* mRNA, and that this is associated with corresponding changes at the protein level during differentiation of C2C12 cells (Supplementary Fig. S4b). This may suggest that expression of CUGBP1 and MBNL1 are mutually regulated in myogenic differentiation. Kuyumcu-Martinez and colleagues report that expanded CUG repeats of *DMPK* through an unknown mechanism leads to phosphorylation and thereby to stabilization of CUGBP1 in DM1 myoblasts[10]. Our studies additionally suggest that loss of MBNL1 in DM1 could lead to decreased decay of *CUGBP1* mRNA and hence to further increase of CUGBP1 activity. Although CUGBP1 is not upregulated in adult MBNL1-knockout mice, this mechanism could lead to increased misregulation of splicing and decay of the mRNAs of target genes in embryonic development that culminates in the DM1 phenotype.

We find that binding sites for CUGBP1 and MBNL1 are enriched around alternative cassette exons (Fig. 2a). The binding sites for CUGBP1 are prominent in adjacent intronic regions flanking alternative exons. Our functional analysis reveals that binding of CUGBP1 to the upstream intron facilitates exon skipping, whereas

binding to the downstream intron enhances exon inclusion (Fig. 2b). Interestingly, similar regulation of alternative splicing has been observed for NOVA, FOX2 and PTB[30,45,46], indicating the presence of a common underlying mechanism shared by these proteins.

In contrast to CUGBP1, MBNL1 tags are also enriched in coding exons. Until now, splicing *cis*-elements of MBNL1 have been mapped exclusively to introns, and no exonic *cis*-element has been reported to our knowledge[20,23,34,47,48]. Although MBNL1 preferentially binds to exons, MBNL1 binding to introns is enriched at alternative rather than constitutive splice sites (Fig. 2a. This enrichment is diffusely distributed throughout regions harboring 500 nt upstream or downstream of alternative exons, in contrast to the prominent intronic peaks observed for CUGBP1 tags. This could suggest that MBNL1 needs to bind simultaneously to the target exon and adjacent introns to regulate splicing. Functional analysis of MBNL1 reveals that binding of MBNL1 close to the 3′ end of the downstream intron facilitates exon skipping, whereas no characteristic binding pattern is observed for exons included in response to MBNL1 (Fig. 2c). PTB has also been reported to regulate alternative splicing through binding close to the 3′ end of the downstream intron[36]. In contrast to MBNL1, however, binding of PTB to this region promotes exon inclusion. We similarly find binding of PTB to this region in our HITS-CLIP data in MBNL1-regulated exons (Supplementary Fig. S7d). Interestingly, the MBNL1-binding motif is enriched in PTB-regulated exons[46]. MBNL1 may thus compete for binding with other splicing factors like PTB and regulate alternative splicing events.

Post-transcriptional gene expression regulation is crucial to achieve precise developmental and tissue-specific control of cellular processes. Our studies reveal that CUGBP1 and MBNL1 preferentially bind to the 3′ UTRs of mRNAs encoding RNA-binding proteins and transcription factors, which can regulate cell development. During development of murine skeletal muscles, the nuclear level of MBNL1 increases, while that of CUGBP1 decreases[9,12]. Genes with mRNAs that can be bound both by CUGBP1 and MBNL1 are likely to be down-regulated by CUGBP1 in undifferentiated cells. If these genes need to be tightly down-regulated also in differentiated cells, MBNL1 can substitute for CUGBP1 in order to achieve continued destabilization of the target mRNA. We conclude that finely-tuned expression of CUGBP1 and MBNL1 may be important regulators of myogenic differentiation through precise regulation of both alternative splicing and mRNA stability.

Methods

Antibodies. Antibodies to CUGBP1 (3B1), MHC (H300), myogenin (M225) and PTB (N20) were purchased from Santa Cruz Biotechnology. Anti-GAPDH pAb was purchased from Sigma. Anti-PITX2 pAb was purchased from Abcam. Anti-MBNL1 rabbit serum (A2764) was a kind gift of Dr. Charles A. Thornton at University of Rochester. The specificity of antibodies against CUG BP1 and MBNL1 is supported by the data in previous reports 2,3 and also by our siRNA experiments (Supplementary Fig. S1).

Cell culture. Detailed methods are included in the Supplementary Information.

HITS-CLIP. C2C12 cells were UV-irradiated at 400 mJ and CLIP was performed as previously described[49]. High-throughput 36-bp single-end and 40-bp single-end sequencing was performed using an Illumina Genome Analyzer II. All HITS-CLIP data were registered in ArrayExpress with an accession number E-MTAB-414 and in ENA with an accession number ERP000789. Detailed information is provided in the Supplementary Information.

Bioinformatics analysis. Illumina reads were first prepared by removing the 4-bp tag and filtering sequences composed primarily of Illumina adapter. The resulting reads were mapped to the mouse genome (NCBI Build 37.1/mm9) with default parameters using the BWA[50] mapping software. To extract consensus motifs from the mapped reads, we considered only uniquely aligned reads and first removed duplicate reads to avoid potential PCR-mediated deviations in addition to bias from very highly expressed transcripts. We then extended the reads to 110 nt, the expected mean of the CLIP fragments and used the SeqMonk software (www.bioinformatics.bbsrc.ac.uk/projects/seqmonk) to identify binding regions by using the program's built-in peak detection algorithm. Peaks were scored using both a reads per peak scoring scheme and a maximum depth scoring scheme (effectively the height of the peak) in order to filter out peaks. For the identification of CUGBP1- and MBNL1-binding regions, we used PTB as a negative control and removed peaks present in the PTB dataset as well. We then selected CUGBP1 peaks that were present in the two independent CUGBP1 CLIP experiments and MBNL1 peaks that were similarly corroborated by the two MBNL1 experiments. PTB binding regions were identified by removing peaks that were present in either of the four CUGBP1 and MBNL1 experiments. Finally, we restricted the set of binding regions to only those spanning 70–150 bp since this was the fragment length used in the CLIP experiments. We analyzed each dataset using a motif analysis tool, MEME[31], using a background Markov model based on the entire mouse genome.

We analyzed the mapped Illumina reads and binding regions and mapped them to UCSC knownGene annotations[51] of the mouse genome (NCBI Build 37.1/mm9) by writing and running Perl and Excel VBA programs, as well as by running BEDTools utilities[52]. Normalized complexity maps of CUGBP1/MBNL1/PTB-RNA interactions were generated as previously described[30]. For the control, normalized complexity map was similarly generated by analyzing 100 sets of 15 to 50 constitutive exons that were randomly selected from 118,969 constitutive exons in mm9. To identify enriched Gene Ontology terms, we used the Database for Annotation, Visualization and Integrated Discovery (DAVID 6.7)[53,54].

Construction of plasmids. To construct luciferase reporter vectors with the 3′ UTR of *Gapdh* and *Pitx2*, 3′ UTRs of these genes were amplified by PCR. Amplified DNA was ligated into the *Xba*I and *Bam*HI sites of the pGL3-promoter vector (Promega) to substitute for the 3′ UTR of the firefly luciferase gene. DNA fragments harboring GT and CTG repeats were amplified by self-priming PCR using primers terminating in a *Xba*I site, and ligated into the *Xba*I site to make the pGL3P-*Gapdh*-3′ UTR.

To construct tet-responsive luciferase constructs, the tet-responsive promoter region was excised from pTRE-Tight vector (Clontech) with *Xho*I-*Hin*dIII site and cloned into the *Xho*I-*Hin*dIII site of the pGL3-promoter vector with the 3′ UTR of *Gapdh* and *Pitx2*. To introduce mutations in 3′ UTR of *Pitx2* in the luciferase construct, we used the QuikChange site-directed mutagenesis kit (Stratagene).

To construct expression vectors for MBNL1 and CUGBP1, the human MBNL1 cDNA and human CUGBP1 cDNA (Open Biosystems) were subcloned into the mammalian bidirectional expression vector pBI-CMV2 (Clontech), which should constitutively expresses the insert and AcGFP1.

RNA interference and transfection. The siRNA duplexes against CUGBP1 and MBNL1 were synthesized by Sigma. The sense sequences of the siRNAs were as follows: Cugbp1-1, 5′-GCUUUGGUUUUGUAAGUUA-3′; Cugbp1-2, 5′-GGCUUAAAGUGCAGCUCAA-3′; Mbnl1-1, 5′-CACUGGAAGUAUGUAGAGA-3′; and Mbnl1-2, 5′-GCACAAUGAUUGAUACCAA-3′. We purchased the AllStar Negative Control siRNA (1027281) from Qiagen. C2C12 cells were seeded on 24-well plates, and transfected with siRNA using Lipofectamine 2000 (Invitrogen) according to the manufacturer's instructions. Tet-off advanced HEK293 cells were seeded on 96-well plates, and were transfected with luciferase reporter gene constructs using FuGENE 6 (Roche) according to the manufacturer's instructions. At 48 hrs after transfection, cells were either harvested for RNA extraction or processed for isolation of total proteins or nuclear extracts.

RT-PCR for splicing analysis. Total RNA was extracted using Trizol (Invitrogen) according to the manufacturer's instructions. cDNA was synthesized using an oligo-dT primer and ReverTra Ace (Toyobo), and PCR amplifications were performed using GoTaq (Promega) for 30–35 cycles. Sequences of the primers used for PCR are listed in the Supplementary Table S3. The intensities of PCR-amplified spliced products were quantified with the ImageJ 1.42q software (NIH). We then calculated a percentage of exon inclusion (% inclusion) as the ratio of the intensity of the upper band divided by the sum of intensities of all the bands.

Real-time RT-PCR for RNA stability analysis. Total RNA was extracted using RNeasy mini kit (Qiagen) or CellAmp Direct RNA Prep Kit (Takara) according to the manufacturer's instructions. cDNA was synthesized as described above and real-time PCR was performed using the Mx3005P QPCR System (Stratagene) and the SYBR Premix Ex Taq II (Takara). Sequences of the primers used for PCR are listed in Supplementary Table S4.

Microarray analysis. Total RNA was extracted using the RNeasy mini kit according to the manufacturer's instructions. We synthesized and labeled cDNA fragments from 100 ng of total RNA using the GeneChip WT cDNA Synthesis Kit (Ambion). The labeled cDNAs were hybrized to the Affymetrix Mouse Exon 1.0 ST Arrays for splicing analysis or the Affymetrix Mouse Gene 1.0 ST Arrays for analyzing temporal profiles of expression of CUGBP1/MBNL1-targeted genes following the manufacturer's protocols. The robust multichip analysis (RMA) algorithm was used to normalize the array signals across chips with the Affymetrix Expression Console software 1.1.2. All microarray data were uploaded to the Gene Expression Omnibus database (accession numbers, GSE29990 for exon arrays and GSE27583 for expression arrays).

Western blotting. For preparation of total cell lysates, cells were lysed in buffer A (10 mM HEPES pH 7.8, 10 mM KCl, 0.1 mM EDTA, 1 mM DTT, 2 μg/ml Aprotinin, 0.5 mM PMSF, 0.1% NP-40) and incubate on ice for 20 min. After sonication, samples were centrifuged (15,000 rpm, 5 min) and the supernatants were stored at −80°C for further experiments. For preparation of nuclear cell lysates, cells were suspended in 400 μl of buffer A. Nuclei were pelleted, and the cytoplasmic

proteins were carefully removed. The nuclei were then resuspended in buffer C (50 mM HEPES pH 7.8, 420 mM KCl, 0.1 mM EDTA, 5 mM $MgCl_2$, 2% Glycerol, 1 mM DTT, 2 μg/ml Aprotinin, and 0.5 mM PMSF). After vortexing and stirring for 20 min at 4°C, the samples were centrifuged, and the supernatants were stored at −80°C. Samples were analyzed on a 10% SDS polyacrylamide gel, and the proteins were transferred to Immobilon polyvinylidene difluoride membranes (Millipore). Membranes were blocked with 1% BSA in Tris-buffered saline containing 0.05% Tween20 (TBST) for 1 hr, incubated for 1 hr with primary antibodies in TBST, washed three times with TBST, and incubated for 1 hr with horseradish peroxidase-conjugated anti-mouse or -rabbit immunoglobulin (GE) diluted 1 : 5,000 in TBST. After three washes in TBST, the blot was developed with the enhanced chemiluminescence system (GE) according to the manufacturer's instructions.

Luciferase assay. HEK293 cells seeded on a 96 well plate were transfected with 10 ng of pGL3P-*Gapdh*-3′ UTR with or without GT and CTG repeats, 5 ng of pRL/SV40 (Promega), and 40 ng of pBI-CMV2-based CUGBP1 or MBNL1 expression vector using FuGENE 6. At 48 hrs after the transfection, the luciferase activity was measured using the Dual-Luciferase Reporter Assay System (Promega) according to the manufacturer's instructions.

1. Licatalosi, D. D. & Darnell, R. B. RNA processing and its regulation: global insights into biological networks. *Nat Rev Genet* **11**, 75–87 (2010).
2. Wang, G. S. & Cooper, T. A. Splicing in disease: disruption of the splicing code and the decoding machinery. *Nat Rev Genet* **8**, 749–61 (2007).
3. Brook, J. D. *et al.* Molecular basis of myotonic dystrophy: expansion of a trinucleotide (CTG) repeat at the 3′ end of a transcript encoding a protein kinase family member. *Cell* **68**, 799–808 (1992).
4. Day, J. W. & Ranum, L. P. RNA pathogenesis of the myotonic dystrophies. *Neuromuscul Disord* **15**, 5–16 (2005).
5. Larkin, K. & Fardaei, M. Myotonic dystrophy—a multigene disorder. *Brain Res Bull* **56**, 389–95 (2001).
6. Lee, J. E. & Cooper, T. A. Pathogenic mechanisms of myotonic dystrophy. *Biochem Soc Trans* **37**, 1281–6 (2009).
7. Turner, C. & Hilton-Jones, D. The myotonic dystrophies: diagnosis and management. *J Neurol Neurosurg Psychiatry* **81**, 358–67 (2010).
8. Miller, J. W. *et al.* Recruitment of human muscleblind proteins to (CUG)(n) expansions associated with myotonic dystrophy. *EMBO J* **19**, 4439–48 (2000).
9. Lin, X. *et al.* Failure of MBNL1-dependent post-natal splicing transitions in myotonic dystrophy. *Hum Mol Genet* **15**, 2087–97 (2006).
10. Kuyumcu-Martinez, N. M., Wang, G. S. & Cooper, T. A. Increased steady-state levels of CUGBP1 in myotonic dystrophy 1 are due to PKC-mediated hyperphosphorylation. *Mol Cell* **28**, 68–78 (2007).
11. Iwahashi, C. K. *et al.* Protein composition of the intranuclear inclusions of FXTAS. *Brain* **129**, 256–71 (2006).
12. Kalsotra, A. *et al.* A postnatal switch of CELF and MBNL proteins reprograms alternative splicing in the developing heart. *Proc Natl Acad Sci U S A* **105**, 20333–8 (2008).
13. Bland, C. S. *et al.* Global regulation of alternative splicing during myogenic differentiation. *Nucleic Acids Res* (2010).
14. Philips, A. V., Timchenko, L. T. & Cooper, T. A. Disruption of splicing regulated by a CUG-binding protein in myotonic dystrophy. *Science* **280**, 737–41 (1998).
15. Ho, T. H., Bundman, D., Armstrong, D. L. & Cooper, T. A. Transgenic mice expressing CUG-BP1 reproduce splicing mis-regulation observed in myotonic dystrophy. *Hum Mol Genet* **14**, 1539–47 (2005).
16. Savkur, R. S., Philips, A. V. & Cooper, T. A. Aberrant regulation of insulin receptor alternative splicing is associated with insulin resistance in myotonic dystrophy. *Nat Genet* **29**, 40–7 (2001).
17. Charlet, B. N. *et al.* Loss of the muscle-specific chloride channel in type 1 myotonic dystrophy due to misregulated alternative splicing. *Mol Cell* **10**, 45–53 (2002).
18. Begemann, G. *et al.* muscleblind, a gene required for photoreceptor differentiation in Drosophila, encodes novel nuclear Cys3His-type zinc-finger-containing proteins. *Development* **124**, 4321–31 (1997).
19. Teplova, M. & Patel, D. J. Structural insights into RNA recognition by the alternative-splicing regulator muscleblind-like MBNL1. *Nat Struct Mol Biol* **15**, 1343–51 (2008).
20. Ho, T. H. *et al.* Muscleblind proteins regulate alternative splicing. *EMBO J* **23**, 3103–12 (2004).
21. Cass, D. *et al.* The four Zn fingers of MBNL1 provide a flexible platform for recognition of its RNA binding elements. *BMC Mol Biol* **12**, 20 (2011).
22. Kanadia, R. N. *et al.* A muscleblind knockout model for myotonic dystrophy. *Science* **302**, 1978–80 (2003).
23. Fugier, C. *et al.* Misregulated alternative splicing of BIN1 is associated with T tubule alterations and muscle weakness in myotonic dystrophy. *Nature Medicine* **17**, 720–5 (2011).
24. Moraes, K. C., Wilusz, C. J. & Wilusz, J. CUG-BP binds to RNA substrates and recruits PARN deadenylase. *Rna* **12**, 1084–91 (2006).
25. Vlasova, I. A. *et al.* Conserved GU-rich elements mediate mRNA decay by binding to CUG-binding protein 1. *Mol Cell* **29**, 263–70 (2008).
26. Lee, J. E., Lee, J. Y., Wilusz, J., Tian, B. & Wilusz, C. J. Systematic analysis of cis-elements in unstable mRNAs demonstrates that CUGBP1 is a key regulator of mRNA decay in muscle cells. *PLoS One* **5**, e11201 (2010).
27. Rattenbacher, B. *et al.* Analysis of CUGBP1 Targets Identifies GU-Repeat Sequences That Mediate Rapid mRNA Decay. *Mol Cell Biol* **30**, 3970–80 (2010).
28. Timchenko, N. A., Iakova, P., Cai, Z. J., Smith, J. R. & Timchenko, L. T. Molecular basis for impaired muscle differentiation in myotonic dystrophy. *Mol Cell Biol* **21**, 6927–38 (2001).
29. Timchenko, N. A. *et al.* Overexpression of CUG triplet repeat-binding protein, CUGBP1, in mice inhibits myogenesis. *J Biol Chem* **279**, 13129–39 (2004).
30. Licatalosi, D. D. *et al.* HITS-CLIP yields genome-wide insights into brain alternative RNA processing. *Nature* **456**, 464–9 (2008).
31. Bailey, T. L. & Elkan, C. The value of prior knowledge in discovering motifs with MEME. *Proc Int Conf Intell Syst Mol Biol* **3**, 21–9 (1995).
32. Marquis, J. *et al.* CUG-BP1/CELF1 requires UGU-rich sequences for high-affinity binding. *Biochem J* **400**, 291–301 (2006).
33. Du, H. *et al.* Aberrant alternative splicing and extracellular matrix gene expression in mouse models of myotonic dystrophy. *Nat Struct Mol Biol* **17**, 187–93 (2010).
34. Goers, E. S., Purcell, J., Voelker, R. B., Gates, D. P. & Berglund, J. A. MBNL1 binds GC motifs embedded in pyrimidines to regulate alternative splicing. *Nucleic Acids Res* (2010).
35. Kino, Y. *et al.* Muscleblind protein, MBNL1/EXP, binds specifically to CHHG repeats. *Hum Mol Genet* **13**, 495–507 (2004).
36. Xue, Y. *et al.* Genome-wide analysis of PTB-RNA interactions reveals a strategy used by the general splicing repressor to modulate exon inclusion or skipping. *Mol Cell* **36**, 996–1006 (2009).
37. Hamada, H., Meno, C., Watanabe, D. & Saijoh, Y. Establishment of vertebrate left-right asymmetry. *Nat Rev Genet* **3**, 103–13 (2002).
38. Yashiro, K., Shiratori, H. & Hamada, H. Haemodynamics determined by a genetic programme govern asymmetric development of the aortic arch. *Nature* **450**, 285–8 (2007).
39. Dong, F. *et al.* Pitx2 promotes development of splanchnic mesoderm-derived branchiomeric muscle. *Development* **133**, 4891–9 (2006).
40. Shih, H. P., Gross, M. K. & Kioussi, C. Cranial muscle defects of Pitx2 mutants result from specification defects in the first branchial arch. *Proceedings of the National Academy of Sciences of the United States of America* **104**, 5907–12 (2007).
41. Gherzi, R. *et al.* Akt2-mediated phosphorylation of Pitx2 controls Ccnd1 mRNA decay during muscle cell differentiation. *Cell Death and Differentiation* **17**, 975–83 (2010).
42. Chen, H. H., Xu, J., Safarpour, F. & Stewart, A. F. LMO4 mRNA stability is regulated by extracellular ATP in F11 cells. *Biochem Biophys Res Commun* **357**, 56–61 (2007).
43. Zhang, L., Lee, J. E., Wilusz, J. & Wilusz, C. J. The RNA-binding protein CUGBP1 regulates stability of tumor necrosis factor mRNA in muscle cells: implications for myotonic dystrophy. *J Biol Chem* **283**, 22457–63 (2008).
44. Horb, L. D. & Horb, M. E. BrunoL1 regulates endoderm proliferation through translational enhancement of cyclin A2 mRNA. *Dev Biol* (2010).
45. Yeo, G. W. *et al.* An RNA code for the FOX2 splicing regulator revealed by mapping RNA-protein interactions in stem cells. *Nat Struct Mol Biol* **16**, 130–7 (2009).
46. Llorian, M. *et al.* Position-dependent alternative splicing activity revealed by global profiling of alternative splicing events regulated by PTB. *Nat Struct Mol Biol* **17**, 1114–23 (2010).
47. Hino, S. *et al.* Molecular mechanisms responsible for aberrant splicing of SERCA1 in myotonic dystrophy type 1. *Hum Mol Genet* **16**, 2834–43 (2007).
48. Sen, S. *et al.* Muscleblind-like 1 (Mbnl1) promotes insulin receptor exon 11 inclusion via binding to a downstream evolutionarily conserved intronic enhancer. *J Biol Chem* **285**, 25426–37 (2010).
49. Ule, J., Jensen, K., Mele, A. & Darnell, R. B. CLIP: a method for identifying protein-RNA interaction sites in living cells. *Methods* **37**, 376–86 (2005).
50. Li, H. & Durbin, R. Fast and accurate long-read alignment with Burrows-Wheeler transform. *Bioinformatics* **26**, 589–95 (2010).
51. Rhead, B. *et al.* The UCSC Genome Browser database: update 2010. *Nucleic Acids Res* **38**, D613–9 (2010).
52. Quinlan, A. R. & Hall, I. M. BEDTools: a flexible suite of utilities for comparing genomic features. *Bioinformatics* **26**, 841–2 (2010).
53. Huang da, W., Sherman, B. T. & Lempicki, R. A. Systematic and integrative analysis of large gene lists using DAVID bioinformatics resources. *Nat Protoc* **4**, 44–57 (2009).
54. Dennis, G., Jr. *et al.* DAVID: Database for Annotation, Visualization, and Integrated Discovery. *Genome Biol* **4**, P3 (2003).

Acknowledgements

This work was supported by a JST-DASTI joint grant entitled "Strategic Japanese-Danish Cooperative Program on Molecular Medical Research", by Grants-in-Aid from the MEXT and MHLW of Japan, and by a grant from the Danish Medical Research Council (FSS Grant no. 271-07-342).

Author contributions

A.M., H.S.A, T.O., and M.I. performed the experiments. A.M., T.K.D., B.S.A., and K.O. analyzed the data. A.M., T.K.D., B.S.A. and K.O. prepared the manuscript. All authors reviewed the manuscript.

Additional information

Accession codes: All HITS-CLIP data were registered in ArrayExpress with an accession number E-MTAB-414 and in ENA with an accession number ERP000789.

All microarray data were uploaded to the Gene Expression Omnibus database with accession numbers, GSE29990 for exon arrays and GSE27583 for expression arrays.

Supplementary information accompanies this paper at http://www.nature.com/scientificreports

Competing financial interests: The authors declare no competing financial interests.

How to cite this article: Masuda, A. *et al.* CUGBP1 and MBNL1 preferentially bind to 3′ UTRs and facilitate mRNA decay. *Sci. Rep.* **1**, 209; DOI:10.1038/srep00209 (2011).

ARTICLE IN PRESS
JNS-12138; No of Pages 5
Journal of the Neurological Sciences xxx (2012) xxx–xxx
Contents lists available at SciVerse ScienceDirect
Journal of the Neurological Sciences
journal homepage: www.elsevier.com/locate/jns

A novel mutation in SCN4A causes severe myotonia and school-age-onset paralytic episodes

Harumi Yoshinaga [a,*], Shunichi Sakoda [b], Jean-Marc Good [c], Masanori P. Takahashi [c], Tomoya Kubota [c], Eri Arikawa-Hirasawa [d], Tomohiko Nakata [e], Kinji Ohno [e], Tetsuro Kitamura [f], Katsuhiro Kobayashi [a], Yoko Ohtsuka [a]

[a] Department of Child Neurology, Okayama University Graduate School of Medicine, Dentistry, and Pharmaceutical Sciences, Okayama, Japan
[b] Department of Neurology, Kagoshima University Graduate School of Medical and Dental Sciences, Medical School, Kagoshima, Japan
[c] Department of Neurology, Osaka University Graduate School of Medicine, Osaka, Japan
[d] Department of Neurology, Juntendo University School of Medicine, Tokyo, Japan
[e] Division of Neurogenetics, Center for Neurological Diseases and Cancer, Nagoya University Graduate School of Medicine, Aichi, Japan
[f] Department of Pediatrics, Nipponkokan Fukuyama Hospital, Hiroshima, Japan

ARTICLE INFO

Article history:
Received 27 June 2011
Received in revised form 30 November 2011
Accepted 22 December 2011
Available online xxxx

Keywords:
Channelopathy
Na channel
Skeletal muscle
Activation
Slow inactivation
Schwarz–Jampel syndrome
SCN4A

ABSTRACT

Mutations in the pore-forming subunit of the skeletal muscle sodium channel (*SCN4A*) are responsible for hyperkalemic periodic paralysis, paramyotonia congenita and sodium channel myotonia. These disorders are classified based on their cardinal symptoms, myotonia and/or paralysis. We report the case of a Japanese boy with a novel mutation of *SCN4A*, p.I693L, who exhibited severe episodic myotonia from infancy and later onset mild paralytic attack. He started to have apneic episodes with generalized hypertonia at age of 11 months, then developed severe episodic myotonia since 2 years of age. He presented characteristic generalized features which resembled Schwarz–Jampel syndrome. After 7 years old, paralytic episodes occurred several times a year. The compound muscle action potential did not change during short and long exercise tests. Functional analysis of the mutant channel expressed in cultured cell revealed enhancement of the activation and disruption of the slow inactivation, which were consistent with myotonia and paralytic attack. The severe clinical features in his infancy may correspond to myotonia permanence, however, he subsequently experienced paralytic attacks. This case provides an example of the complexity and overlap of the clinical features of sodium channel myotonic disorders.

1. Introduction

To date, over 40 different mutations causing Na channelopathies of the skeletal muscle have been reported in *SCN4A* gene, which encodes for the pore-forming alpha-subunit of skeletal muscle sodium channel [1,2]. The Na channelopathies of the skeletal muscle are clinically classified into hyperkalemic periodic paralysis, paramyotonia congenita, or sodium channel myotonia on the basis of their clinical phenotype. However, phenotypic variability and marked overlap in symptoms have been reported [3–6]. The cases with severe phenotype in the neonatal period highlight the high clinical variability of sodium channelopathies [7,8]. The electrophysiological studies using heterologously expressed channels have shown that the missense mutations produces a gain-of-function defect of the fast gating such as disrupted fast inactivation and enhanced activation, which should result in increased excitability of the muscle membrane. It has been revealed that not only the defect of fast gating but also that of slow inactivation predisposes to paralytic attack, one of the clinical features of Na channelopathies [9,10].

In this report, we present a Japanese boy with skeletal dysplasia who exhibited very severe myotonia in infancy and mild paralytic attack after seven years of age. We identified a novel mutation in the intracellular loop linking segments 4–5 of domain II in *SCN4* and found that the heterologously expressed mutant channel showed enhancement of the activation and disruption of the slow inactivation.

2. Case report

2.1. Clinical features

The patient was delivered naturally and without complications. There is no family history of neuromuscular disease. Seven days after birth, he experienced transient breath-holding episodes with generalized muscle stiffness and facial pallor while crying. At 11 months of age, 30-second-long episodes of apnea arose with

* Corresponding author at: Shikatacho 2-5-1 Department of Child Neurology, Okayama University Graduate School of Medicine, Dentistry, and Pharmaceutical Sciences, Okayama 700–8558 Japan. Tel.: +81 86 235 7372; fax: +81 86 235 7377.
E-mail address: magenta@md.okayama-u.ac.jp (H. Yoshinaga).

0022-510X/$ – see front matter © 2012 Elsevier B.V. All rights reserved.
doi:10.1016/j.jns.2011.12.015

generalized hypertonia; these episodes were so severe that epileptic seizures were once suspected, but ictal EEG recordings did not indicate that this was the case. These episodes spontaneously disappeared, but at the age of two, the patient started to present daily fluctuating myotonia. The patient presented with a mask-like face with blepharospasm, grip myotonia, and dysarthria. These episodic myotonic attacks persisted for several minutes, hours, or even days, with fluctuation and created difficulties in standing, walking and upper-limb mobility. The symptoms seemed to be aggravated by cold (and were relieved during febrile illness) and fatigue, but not by potassium intake or exercise. The CK value fluctuated between 200 and 1000+ and tended to be high during myotonic attacks.

Fig. 1 depicts a generalized inter-episode feature when he was 5 years and 8 months old. Parental consent to present the photograph in Fig. 1 was obtained. He was of Herculean stature and exhibited several characteristic features, such as low-set ears, epicanthic folds, upturned nose, a long philtrum, puckered lips, short neck, hypertropic thighs, atrophic shoulder girdle muscles, pigeon breast, and joint contracture of the elbow. Accordingly, he was initially suspected as having a myogenic type of Schwarz–Jampel syndrome [4,11]. However, immunofluorescence stain for perlecan was normal in biopsied muscle and the histology revealed a nonspecific myopathic change with increased fiber variability. Acetazolamide, mexiletine, and phenytoin had some effect on his myotonic attacks. When these medications were discontinued on the day he underwent generalized anesthesia for the muscle biopsy, he experienced a very severe myotonic attack that involved the respiratory muscle.

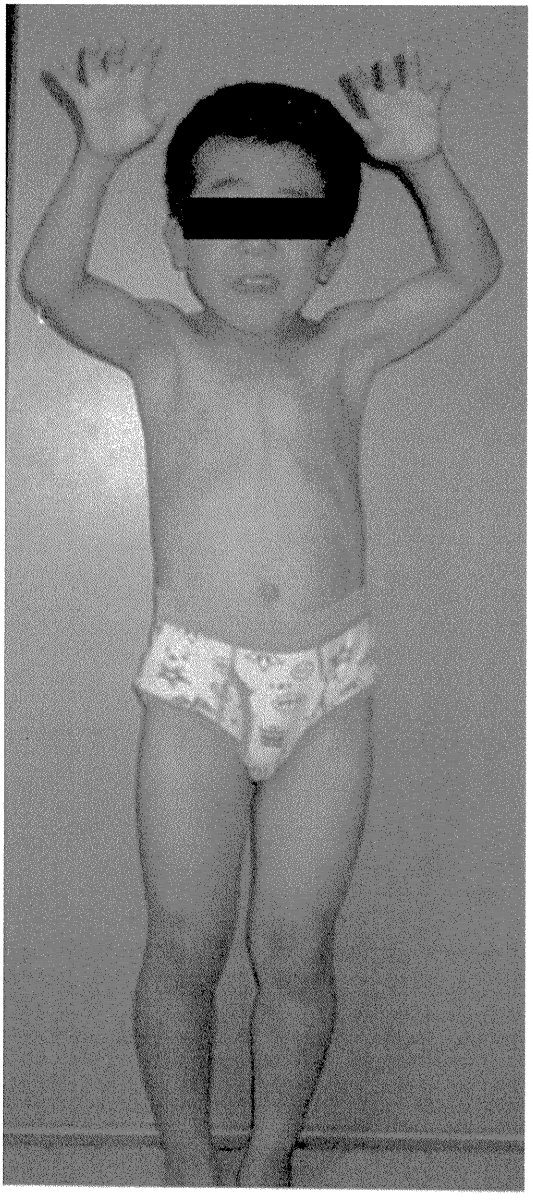

Fig. 1. The patient at 5 years and 8 months of age. Note his Herculean stature and hypertrophic thighs.

After 7 years and 8 months of age, paralytic episodes appeared that occurred several times a year thereafter, even in hot summertime temperatures. He complained of muscle weakness lasting from hours to several days at a time. His mother observed that his thighs become unusually soft during episodes. Neither exercise nor cooling brought about his episodic weakness.

2.2. Clinical electrophysiological analysis

Needle electromyography revealed diffuse continuous myotonic discharges accentuated by needle displacement with dive bomber sounds. Analysis of the compound muscle action potential (CMAP) amplitude before and after short or long exercise revealed no significant change [12]. Muscle cooling did not affect the CMAP either [13].

2.3. DNA analysis

Since there was no expansion of the repeat length at the DM1 locus with Southern blot, we analyzed the nucleotide sequence of *SCN4A* and *CLCN1* genes. Written informed consent was obtained from the parents for the mutation screening. This study was approved by the ethics committee of Kagoshima University Graduate School of Medical and Dental Sciences. Nucleotide sequence analysis of the patient's DNA showed a transition of A to C at the nucleotide in position 2077 (c.2077A>C) in *SCN4A* resulting in the substitution of isoleucine to leucine at amino acid in position 693 (p.I693L) (Fig. 2A). This mutation was not found in the DNA of the parents, both of whom were clinically non-affected. No mutations of *CLCN1* genes were identified by sequencing analysis.

Furthermore, the possibility of Schwarz–Jampel syndrome was excluded by re-sequencing all the exons and the flanking intronic regions of *HSPG2*. We enriched exonic fragments using the SureSelect Human All Exon v2 kit (Agilent, CA, USA), and read 50-bp fragments with the ABI SOLiD 4 sequencer (Applied Biosystems, CA, USA). We mapped 56,007,335 tags (89% of total tags) to human genome GRCh37.3/hg19 with BioScope 1.3.1 (Applied Biosystems), and read 2338 Mbp. Detection of SNVs with Avadis NGS (Strand Life Sciences, Bangalore, India) using default parameters revealed three homozygous missense SNPs that were all registered in dbSNP134 without any reference to clinical relevance (W71S, rs2254357, global minor allelic frequency (GMAF) = 0.475; G242V, rs2254358, GMAF = 0.476; and N765S, rs989994, GMAF = 0.068).

2.4. Sodium channel functional study

We cultured human embryonic kidney (HEK) cells and transfected them with wild-type or mutant human sodium channel constructs as previously described [14]. Na + currents were recorded by the conventional whole-cell patch clamp technique. As shown in Fig. 3A, the mutant channels were consistently activated at more hyperpolarized voltages than the wild-type channels. To further investigate this phenomenon, the normalized sodium conductance at each measured peak current was calculated and plotted against the corresponding voltage. There was a marked shift towards hyperpolarized voltages in the activation curve of p.I693L mutant channels indicating an enhancement of the activation (Fig. 3B. Table 1).

Please cite this article as: Yoshinaga H, et al, A novel mutation in SCN4A causes severe myotonia and school-age-onset paralytic episodes, J Neurol Sci (2012), doi:10.1016/j.jns.2011.12.015

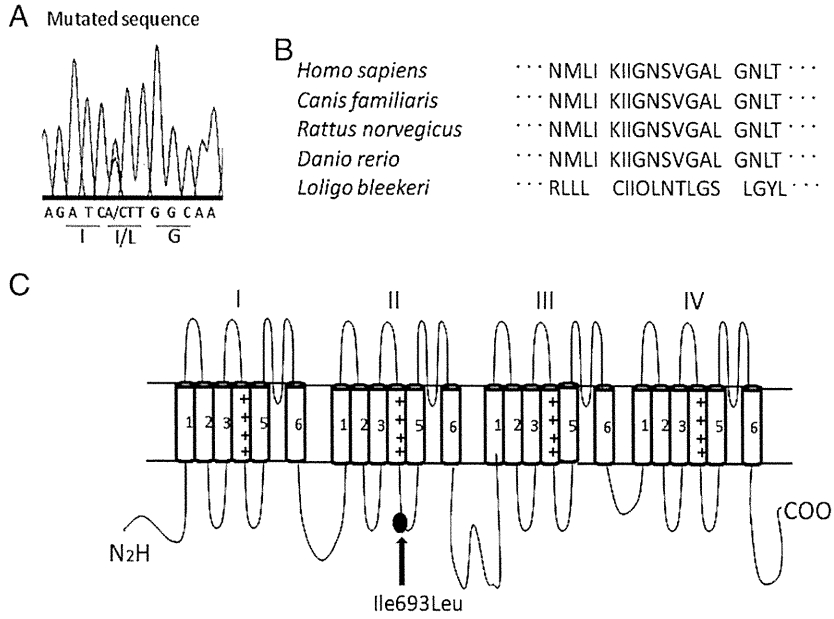

Fig. 2. A: DNA sequencing of the mutant region shows the transition of A to C at the nucleotide in position 2077 resulting in the substitution isoleucine (I) to leucine (L) at aminoacid in position 693 (I693L).B: Isoleucine residue in position 693 in Nav1.4 channel is preserved among homologs in many species.C: Schematic of the α subunit of Nav1.4 channel showing the six transmembrane segments (1–6) of each of the four domains (I–IV) and the location of p.I693L mutation (gray point).

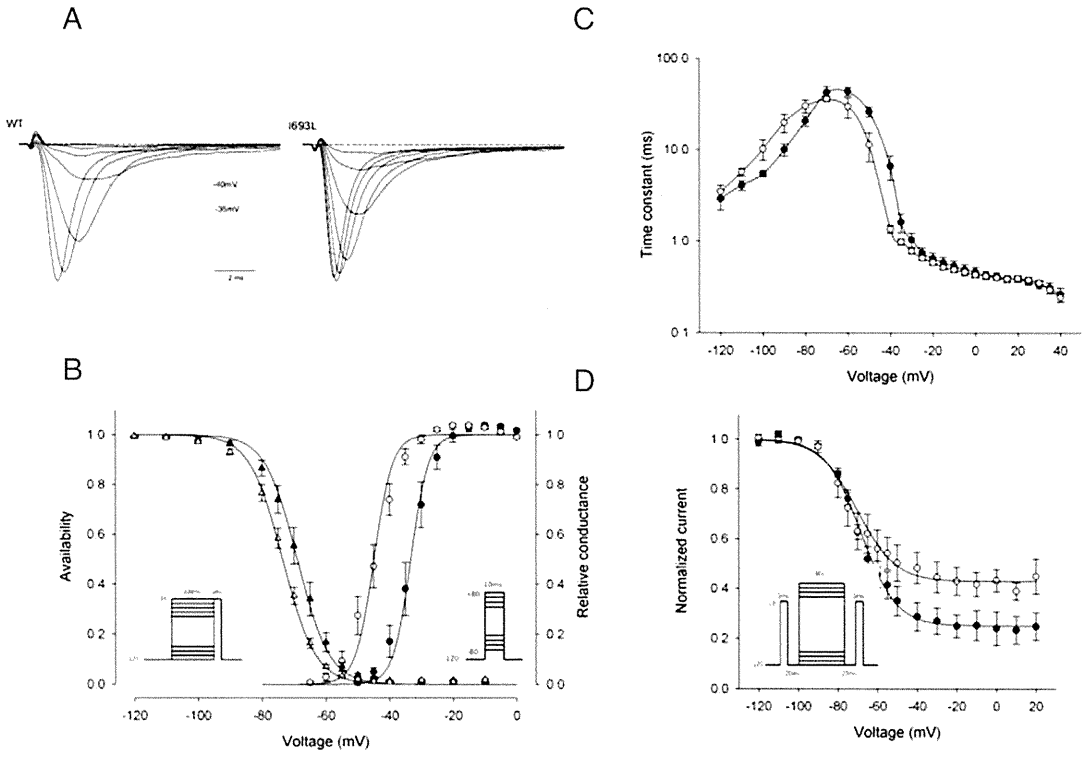

Fig. 3. A: Representative normalized currents recorded from HEK cells transfected with wild-type (WT) and I693L mutant channel and elicited by a series of 10 ms step pulse depolarizations from a holding potential of −120 mV to +40 mV in 5 mV increments. Activation is enhanced in I693L mutant channels.B: Activation (right-hand curves) for the wild-type ○ and I693L ● channels measured as the relative conductance of the peak sodium current elicited by depolarizing pulse from a holding potential of −120 mV to +40 mV (protocol in right inset). The activation voltage dependence of I693L mutant was shifted in the direction of hyperpolarization ($p<0.001$). Steady state fast inactivation (left-hand curves) for the wild-type △ and p.I693L ▲ channels measured as the relative peak current elicited by a −10 mV pulse after a 300 ms conditioning (protocol in left inset). We observed a shift towards negative voltages of the mutant constructs ($p=0.009$).C: Voltage dependence of the fast inactivation kinetics for the wild-type ○ and I693L ● channels measured by combining the data from three protocols (see results): a two-pulse recovery protocol (−120 mV to −80 mV), a two-pulse entry protocol (−70 mV to −40 mV) and a single-pulse relaxation protocol (−35 mV to +40 mV). The time constant for I693L channels was slightly slower at the negative voltages measured with the recovery protocol (n.s. $p>0.05$) and faster at the intermediate voltages measured with the entry protocol (from −50 mV to −35 mV $p<0.05$) than the wild-type. No difference was observed at more depolarized voltage.D: Peak sodium current elicited by a −10 mV test pulse was measured after a 60 s conditioning followed by a 20 ms gap at −120 mV to allow recovery from fast inactivation (protocol in the inset). The maximum extent of slow inactivation (1–I0) was smaller for I693L channels ●, revealing its impairment in comparison with the wild-type ○.

Please cite this article as: Yoshinaga H, et al, A novel mutation in SCN4A causes severe myotonia and school-age-onset paralytic episodes, J Neurol Sci (2012), doi:10.1016/j.jns.2011.12.015

Table 1
Gating parameter for WT and mutant Nav 1.4.

	Activation		Fast inactivation		Slow inactivation		
	V1/2(mV)	*k* (mV)	V1/2(mV)	*k* (mV)	V1/2(mV)	*k* (mV)	I0
WT	−33.3 ± 1.5 (9)	2.8 ± 0.4	−68.9 ± 1.6 (9)	5.0 ± 0.2	−68.3 ± 1.4 (5)	8.9 ± 1.1	0.25 ± 0.0522
p.I693L	−44.9 ± 1.5** (16)	2.9 ± 0.2	−73.5 ± 0.9* (5)	5.1 ± 0.2	−70.1 ± 3.3 (6)	9.6 ± 1.6	0.43 ± 0.0446*

Values are means + S.E.M, with number of experiments in parenthesis * significantly different from WT. P<0.05.
**significantly different from WT. P<0.001.

3. Discussion

Prior to identification of the sodium channel mutation, this patient was initially diagnosed as having a myogenic type of Schwartz–Jampel syndrome because of his characteristic appearance with severe myotonia [1,11]. The confusion between Schwartz–Jampel syndrome and sodium channelopathy was previously reported in a patient with myotonia permanence caused by G1306E mutation of SCN4A [4]. Our patient may also correspond to myotonia permanence, and he exhibited severe myotonic symptoms as apneic episodes from the neonatal period. Several patients with a *SCN4A* mutation, who showed severe symptoms including respiratory distress from an early neonatal period have also been reported [7,8]. One of these cases resembled Schwartz–Jampel syndrome [8].

Our patient showed severe myotonic episodes in his early infancy and then subsequent paralytic episodes. This case provides an example of the complexity and overlap of the clinical features of the sodium channel myotonic disorders, which sometimes make their classification difficult.

Some medications, including local anesthetics, anticonvulsants, and antiarrhythmics such as mexiletine, have shown efficacy for myotonic sodium channelopathies by blocking the sodium channel [2,15]. A carbonic anhydrase inhibitor, acetazolamide, is known to prevent paralytic attack but its antimyotonic action is in question. The myotonia of our patient showed a good response to mexiletine, phenytoin and acetazolamide, although carmabazepin showed little effect. Further studies are needed to understand the difference in efficacy between these drugs and the effects of acetazolamide.

The recently proposed standardized protocols involving short and long exercise tests in electromyographic analysis have improved the diagnosis of the subgroup of mutations in muscle channelopathies [12,13]. Fournier et al. [13] reported that combining the responses to several tests defined five electromyographic patterns that correspond to the subgroups of mutations. We applied their protocol to our patient and defined the response as pattern III [11] in which excitability is not impeded by any of the exercise trials. In their report [11], patients carrying G1306A or I693T (same locus on Nav 1.4 as ours [16]) sodium channel mutation also exhibited pattern III.

Functional analysis of the mutant channel revealed that the activation of the mutant channel was markedly enhanced in concordance with the enhanced excitability of our patient. However hyperpolarized shift of the steady-state inactivation curve which should reduce excitability, was also in a milder way observed in the mutant channel. The former may prevail over the latter, explaining the enhanced excitability which contributes to myotonia. Other mutations such as V445M [17], L689I [18], I704M, including the aforementioned I693T [16], have been found to similarly enhance both activation and fast inactivation and are often associated with myotonia.

Also, our data showed disrupted slow inactivation in the mutant construct, a defect which is expected to predispose to prolonged attack of paralysis. Our patient started to show episodic weakness recently. Again, I693T mutation showed an enhancement of activation with a slight shift towards hyperpolarized voltages for the steady state inactivation as well as a severely impaired slow inactivation [16]. The channel gating defects for I693T and its electromyographic pattern are strikingly similar with those observed for I693L. Unexpectedly, the I693T patient suffered from cold-induced weakness with a very mild myotonia [16]. The difference in hydrophobicity between the two mutated amino acids or the underlining genetic or environmental factors such as drug treatment can possibly modulate the expression of the disease.

Two other mutations, L689I and T70M, have been reported in the intracellular loop linking segments 4–5 of domain II in *SCN4A* [18]. Both have a phenotype of hyperkalemic periodic paralysis with a predominant weakness. The functional analysis of these mutant channels again revealed an enhancement of activation, and an impaired slow inactivation to a similar extent as for I693L mutant. These data and ours confirm the fact that the IIS4-S5 linker is one of the determinant regions for the sodium channel slow inactivation and to a various extent for the activation.

4. Conclusion

Further study of the genotype–phenotype correlations through individual cases will increase our knowledge of the variability of signs in this group of diseases and may also provide us with deeper insight into the function of the various regions of sodium channel proteins.

Acknowledgement

We thank Dr. Steve Cannon, University of Texas, for providing the expression vectors. This study was supported by Grants-in-Aids from the Ministry of Education, Culture, Sports, Science and Technology as well as the Ministry of Health, Labor and Welfare of Japan.

References

[1] Lehmann-Horn F, Rudel R, Jurkat-rott K. Nondystrophic myotonias and periodic paralyses. In: Engel AG, Franzini-Armstrong C, editors. Myology. 3rd ed. New York: McGraw Hill; 2004. p. 1257–300.
[2] Matthews E, Fialho D, Tan SV, Venamce SL, Cannon SC, Sternberg D, et al. The non-dystrophic myotonicas: molecular pathogenesis, diagnosis and treatment. Brain 2010;133:9–12.
[3] Plassart E, Eymard B, Maurs L, Hauw JJ, Lyon-Caen O, Fardeau M. Paramyotonia congenita: genotype to phenotype correlations in two families and report of a new mutation in the sodium channel gene. J Neurol Sci 1996;142:126–33.
[4] Colding-Jorgensen E, Duno M, Vissing J. Autosomal dominant monosymptomatic myotonia premanens. Neurology 2006;67:153–5.
[5] Lerche BH, Heine R, Pika U, George Jr AL, Mitovic N, Browatzki M, et al. Human sodium channel myotonia: slowed channel inactivation due to substitutions for a glycine within the III-IV linker. J Physiol 1993;470:13–22.
[6] Rudel R, Ricker K, Lehmann-Horn F. Genotype–phenotype correlations in human skeletal muscle sodium channel diseases. Arch Neurol 1993;50:1241–8.
[7] Lion-Francois L, Mignot C, Vicart S, Manel V, Sternberg D, Landrieu P, et al. Severe neonatal episodic laryngospasm due to de novo SCN4A mutation. Neurology 2010;75:641–5.
[8] Gay S, Dupuis D, Faovre L, Masurel-Paulet A, Labenne M, Colombani M, et al. Severe neonatal non-dystrophic myotonia secondary to a novel mutation of the voltage-gated sodium channel (SCN4A) gene. Am J Med Genet A 2008;146:380–3.
[9] Goldin AL. Mechanisms of sodium channel inactivation. Curr Opin Neurobiol 2003;13(3):284–90.
[10] Hayward LJ, Sandoval GM, Cannnon SC. Defective slow inactivation of sodium channels contributes to familial periodic paralysis. Neurology 1999;52:1447–53.

Please cite this article as: Yoshinaga H, et al, A novel mutation in SCN4A causes severe myotonia and school-age-onset paralytic episodes, J Neurol Sci (2012), doi:10.1016/j.jns.2011.12.015

[11] Topaloglu BH, Serdaroglu A, Okan M, Gucuyener K, Tope M. Improvement of myotonia with carbamazepine in three cases with the Schwartz–Jampel syndrome. Neuropediatrics 1993;24:232–4.
[12] Fournier E, Arzel M, Sternberg D, Vicart S, Laforet P, Eymard B, et al. Electromyography guides toward subgroups of mutations in muscle channelopathies. Ann Neurol 2004;56:650–61.
[13] Fournier E, Viala K, Gervais H, Sternberg D, Arzel M, Vicart S, et al. Cold extends electromyography distinction between ion channel mutations causing myotonia. Ann Neurol 2006;60:356–65.
[14] Hayward LJ, Brown Jr RH, Cannon SC. Inactivation defects caused by myotonia-associated mutations in the sodium channel III–IV linker. J Gen Physiol 1996;107:559–76.
[15] Heatwole CR, Moxley III RT. The nondystrophic myotonia. Neurotherapeutics 2007;4:238–51.
[16] Plassart-Schiess E, Lhuillier L, George Jr AL, Fontaine B, Tabti N. Functional expression of the Ile693Thr Na+ channel mutation associated with paramyotonia congenital in a human cell line. J Physiol 1998;507(3):721–7.
[17] Takahashi MP, Cannon SC. Enhanced slow inactivation by V 445M: a sodium channel mutation associated with myotonia. Biophys J 1999;76:861–8.
[18] Bendahhou S, Cummins TR, Kula RW, Fu YH, Ptacek LJ. Impairment of slow inactivation as a common mechanism for periodic paralysis in DIIS4-S5. Neurology 2002;58:1266–72.

Please cite this article as: Yoshinaga H, et al, A novel mutation in SCN4A causes severe myotonia and school-age-onset paralytic episodes, J Neurol Sci (2012), doi:10.1016/j.jns.2011.12.015

Myasthenic syndrome caused by plectinopathy

D. Selcen, MD
V.C. Juel, MD
L.D. Hobson-Webb, MD
E.C. Smith, MD
D.E. Stickler, MD
A.V. Bite, BS
K. Ohno, MD, PhD
A.G. Engel, MD

Address correspondence and reprint requests to Dr. Andrew G. Engel, Department of Neurology, Mayo Clinic, Rochester, MN 55905
age@mayo.edu

ABSTRACT

Background: Plectin crosslinks intermediate filaments to their targets in different tissues. Defects in plectin cause epidermolysis bullosa simplex (EBS), muscular dystrophy (MD), and sometimes pyloric atresia. Association of EBS with a myasthenic syndrome (MyS) was documented in a single patient in 1999.

Objectives: To analyze the clinical, structural, and genetic aspects of a second and fatal case of EBS associated with a MyS and search for the genetic basis of the disease in a previously reported patient with EBS-MD-MyS.

Methods: Clinical observations; histochemical, immunocytochemical, and electron microscopy studies of skeletal muscle and neuromuscular junction; and mutation analysis.

Results: An African American man had EBS since early infancy, and progressive muscle weakness, hyperCKemia, and myasthenic symptoms refractory to therapy since age 3 years. Eventually he became motionless and died at age 42 years. At age 15 years, he had a marked EMG decrement, and a reduced miniature endplate potential amplitude. The myopathy was associated with dislocated muscle fiber organelles, structurally abnormal nuclei, focal plasmalemmal defects, and focal calcium ingress into muscle fibers. The neuromuscular junctions showed destruction of the junctional folds, and remodeling. Mutation analysis demonstrated a known p.Arg2319X and a novel c.12043dupG mutation in *PLEC1*. The EBS-MD-MyS patient reported in 1999 also carried c.12043dupG and a novel p.Gln2057X mutation. The novel mutations were absent in 200 Caucasian and 100 African American subjects.

Conclusions: The MyS in plectinopathy is attributed to destruction of the junctional folds and the myopathy to defective anchoring of muscle fiber organelles and defects in sarcolemmal integrity. *Neurology*® 2011;76:327-336

GLOSSARY

Ab = antibodies; **AChR** = acetylcholine receptor; **anti-C Ab** = antibody recognizing the C-terminal plectin domain; **anti-Rod Ab** = antibody recognizing the plectin rod domain; **EBS** = epidermolysis bullosa simplex; **EP** = endplate; **IF** = intermediate filament; **IgG** = immunoglobulin G; **MD** = muscular dystrophy; **MyS** = myasthenic syndrome; **P1** = patient 1; **P2** = patient 2.

Plectin is a ~500 kDa dumbbell-shaped molecule with a central coiled-coil rod domain flanked by globular N- and C-terminal domains. Owing to tissue and organelle-specific transcript isoforms, plectin is a versatile linker of cytoskeletal components to target organelles in cells of different tissues.[1–3] In skeletal muscle, multiple alternatively spliced transcripts of exon preceding common exon 2 link desmin intermediate filaments (IFs) to specific targets: the outer nuclear membrane (isoform 1), the outer mitochondrial membrane (isoform 1b), Z disks (isoform 1 d), and costameres in the sarcolemma (isoform 1f).[3] Plectin is also highly expressed at the neuromuscular junction where it provides crucial structural support for the junctional folds.[4] Plectin deficiency in muscle results in progressive muscular dystrophy (MD).[4–19] Plectin

Supplemental data at www.neurology.org

From the Department of Neurology (D.S., A.V.B., K.O., A.G.E.), Mayo Clinic, Rochester, MN; the Department of Neurology (V.C.J., L.D.H.-W., E.C.S.), Duke University School of Medicine, Durham, NC; and the Department of Neurosciences (D.E.S.), Medical University of South Carolina, Charleston. K.O. is currently affiliated with the Center for Neurological Diseases and Cancer, Nagoya University, Japan.

Study funding: Supported by a grant from the National Institute of Neurological Disorders and Stroke RO1-NS 6277 (A.G.E.) and a research grant from the Muscular Dystrophy Association (A.G.E.).

Disclosure: Author disclosures are provided at the end of the article.

is also highly expressed in intercalated disks in the heart but only a single patient with EBS/MD and cardiomyopathy was identified to date.[18] Plectin deficiency in skin causes epidermolysis bullosa simplex (EBS).[20] Some patients with EBS and MD (EBS-MD) also had symptoms suggesting a myasthenic disorder[9,21–23] but this was not suspected or confirmed by specific studies. The association of EBS-MD with a myasthenic syndrome (MyS) was well-documented in a single patient (P1) in 1999.[4] Although numerous autosomal recessive and one dominant mutation in *PLEC* have been detected,[20] the genetic basis of EBS-MD-MyS in P1 was not identified. We describe our findings in a second patient with EBS-MD-MyS (P2), report additional observations in P1, and identify the genetic basis of the disease in both patients.

METHODS All human studies described here were in accord with the guidelines of the Institutional Review Board of the Mayo Clinic.

Structural observations. Routine histochemical studies on cryostat sections and electron microscopy studies were performed as previously described.[24] Immunoglobulin G and the C3 and C9 complement components were immunolocalized as previously reported.[25,26] We immunolocalized the last 50 C-terminal residues of plectin with 4 μg/mL goat polyclonal C-20 antibody (anti-C Ab), and the plectin rod domain with 4 μg/mL 10F6 mouse monoclonal antibody (anti-Rod Ab) (both from Santa Cruz Biotechnology), followed by 3 μg/mL biotinylated donkey antigoat or antimouse immunoglobulin G (IgG) (Jackson ImmunoResearch Laboratories) and the ABC peroxidase kit (Vector Laboratories). Intrafiber calcium excess was evaluated by the Alizarin red stain.[27] Synaptic contact regions were visualized on fixed, teased muscle fibers by a cytochemical reaction for acetylcholinesterase.[28] The acetylcholine receptor (AChR) and plectin were colocalized at endplates (EPs) with rhodamine-labeled α-bungarotoxin and the plectin anti-Rod Ab followed by fluorescent goat antimouse IgG. EPs were localized for electron microscopy[24] and quantitatively analyzed[29] by established methods. Peroxidase-labeled α-bungarotoxin was used for the ultrastructural localization of AChR.[30]

Molecular genetic studies. Genomic DNA was isolated from blood of P1 and muscle of P2 and mRNA from intercostal muscles of both by standard methods. *PLEC* nucleotides were numbered according to the mRNA sequence (GenBank reference no: NM_000445). We used PCR primer pairs to amplify and directly sequence the 32 exons and flanking noncoding regions of *PLEC* isoform 1 and also first exons of isoforms 1b, 1d, and 1f. We screened for the identified novel mutations in 200 Caucasian and 100 African American control subjects using allele-specific PCR. To estimate expression of the rodless isoform of *PLEC* at the mRNA level, we used real-time PCR and SYBR green I (Roche) with 5′ GTGTCATCCAGGAGTACGTG 3′ as the forward primer in exon 30, 5′ AGCGACAGCAGAGTGACCAT 3′ as the forward primer in exon 31 that encodes the rod domain, 5′ GCCTTCTCCTGCTCGATGAA 3′ as the reverse primer in exon 32 for both forward primers, and *GAPDH* as the housekeeping gene. All experiments were done in triplicate.

RESULTS **Clinical observations.** P1 is an African American woman. Her case was reported in 1999 when she was 23 years of age.[4] In brief, she was diagnosed with EBS as an infant and her myasthenic symptoms began around the age of 9 years. Since 1999, her weakness has worsened so she can now only take a few steps, has dysphagia, is dyspneic on slight exertion and at night, and is resistant to anticholinesterase drugs. However, her skin symptoms are mild, with new skin blisters appearing infrequently.

P2 is an African American man. He was a single child without similarly affected family members. He sucked poorly during infancy but this gradually improved. Since the age of 6 weeks, he had an intermittent vesicular eruption over his skin and oral mucosa and developed nail deformities. He attained his motor milestones on time, but had significant fatigue on exertion since age 3 years. At age 11 years he had difficulty running and rising from the floor and serum creatine kinase level was 827 U/L (normal <60 U/L). Prednisone therapy improved his strength but was discontinued because of abdominal pain. Nystatin therapy for thrush worsened the weakness. At age 12 years, a vastus medialis muscle specimen revealed a myopathy associated with necrotic and regenerating fibers, a sural nerve specimen was normal, and a skin biopsy showed EBS and secondary infection. In 1981, at age 15 years, the patient was evaluated at the Mayo Clinic. He now had reduced muscle bulk, bilateral eyelid ptosis, restricted eye movements, and mild facial and moderately severe diffuse cervical and limb muscle weakness, and was areflexic except at the ankles. Nerve conduction studies were normal. Repetitive stimulation at 2 Hz showed a decremental response (67% in hypothenar muscles) that was partially corrected by IV edrophonium chloride. Serratus anterior and intercostal muscles were biopsied. In vitro electrophysiology study of the intercostal specimen by Dr. Edward Lambert revealed reduction of the mean miniature endplate potential amplitude to 50% of normal; the quantal content of the endplate potential was in the low-normal range. Tests for anti-AChR antibodies were negative. A MyS was diagnosed but therapy with pyridostigmine bromide for a year was of no benefit. The weakness progressed more rapidly throughout adolescence and accelerated after routine illnesses. At age

Figure 1 **Patient photographs**

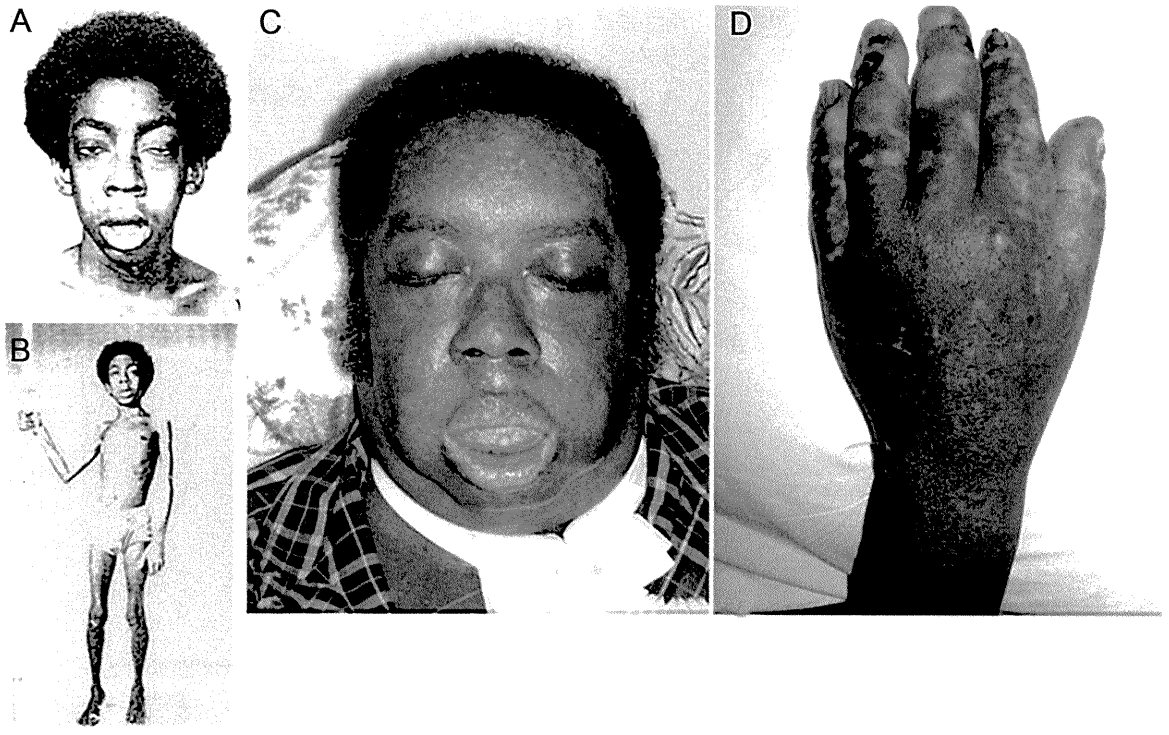

(A, B) Patient at age 17 years. Note severe asymmetric bilateral ptosis, hyperactive frontalis muscle, facial paresis, open mouth, cubitus valgus, Achilles tendon contractures, and diffuse muscle atrophy. (C, D) Patent at age 41 years. He has a tracheostomy, has facial diplegia, is unable to close his mouth or open his eyes, and shows the chronic skin changes of epidermolysis bullosa simplex. He also has blisters on his lip and tongue and oral moniliasis.

17 years, he could barely walk (figure 1, A and B). He was wheelchair-bound by age 18 years, and respirator-dependent by age 26 years. After age 35 years, he had dysarthria and dysphagia and needed a percutaneous gastrostomy. His cognitive functions and cardiac status remained normal. Subsequently, he became motionless (figure 1C), continued to have skin blisters (figure 1D), communicated with clicks and whispers, failed to respond to 3,4-diaminopyridine combined with pyridostigmine bromide, and died of pneumonia at age 42 years.

Histochemistry, P2. Serratus anterior and intercostal muscle specimens showed similar findings (figure 2, A and B). The muscle fiber diameters varied from 6 μm to ~120 μm. There was a mild to moderate increase of internal nuclei. Many nuclei were larger than normal and appeared in subsarcolemmal rows or clusters. Some fibers were necrotic or regenerating or subdividing by splitting, or displayed aberrant myofibrils. There was mild to marked (figure 2B) increase of perimysial and endomysial connective tissue. No immunoglobulin G, C3, or C9 deposits were present at patient endplates. In sections reacted for oxidative enzymes, some fibers showed attenuation or an irregular distribution of enzyme activity. Both muscle specimens showed type 1 fiber preponderance. Because plectin deficiency disconnects or weakens the link between the sarcolemma and the underlying cytoskeleton, it likely increases sarcolemmal vulnerability to mechanical stress. We therefore searched for signs of sarcolemmal injury evidenced by subsarcolemmal calcium deposits[27] and detected these in scattered fibers in both patients (figure 2C and figure e-1 [on the *Neurology*® Web site at www.neurology.org]).

Plectin immunostains. These were performed on 6- to 10-μm-thick acetone fixed frozen sections. In 1999, an antibody recognizing the rod domain of plectin (gift from Dr. Owaribe) showed no immunoreactivity in P1 muscle fibers. As this antibody was no longer available, we used the 10F6 antibody directed against the plectin rod domain (anti-Rod Ab), and a C-20 antibody raised against the last 50 C-terminal residues of plectin (anti-C Ab), and immunolocalized plectin in P1, P2, and normal muscle (see Methods). In normal muscle, both antibodies immunostained the sarcolemma, the intermyofibrillar network, capillaries, and vascular smooth muscle (figure 2, E and H); the C-20 Ab also immunostained perineurium and myelin-

Figure 2 **Histochemistry and plectin localization studies in patient 2**

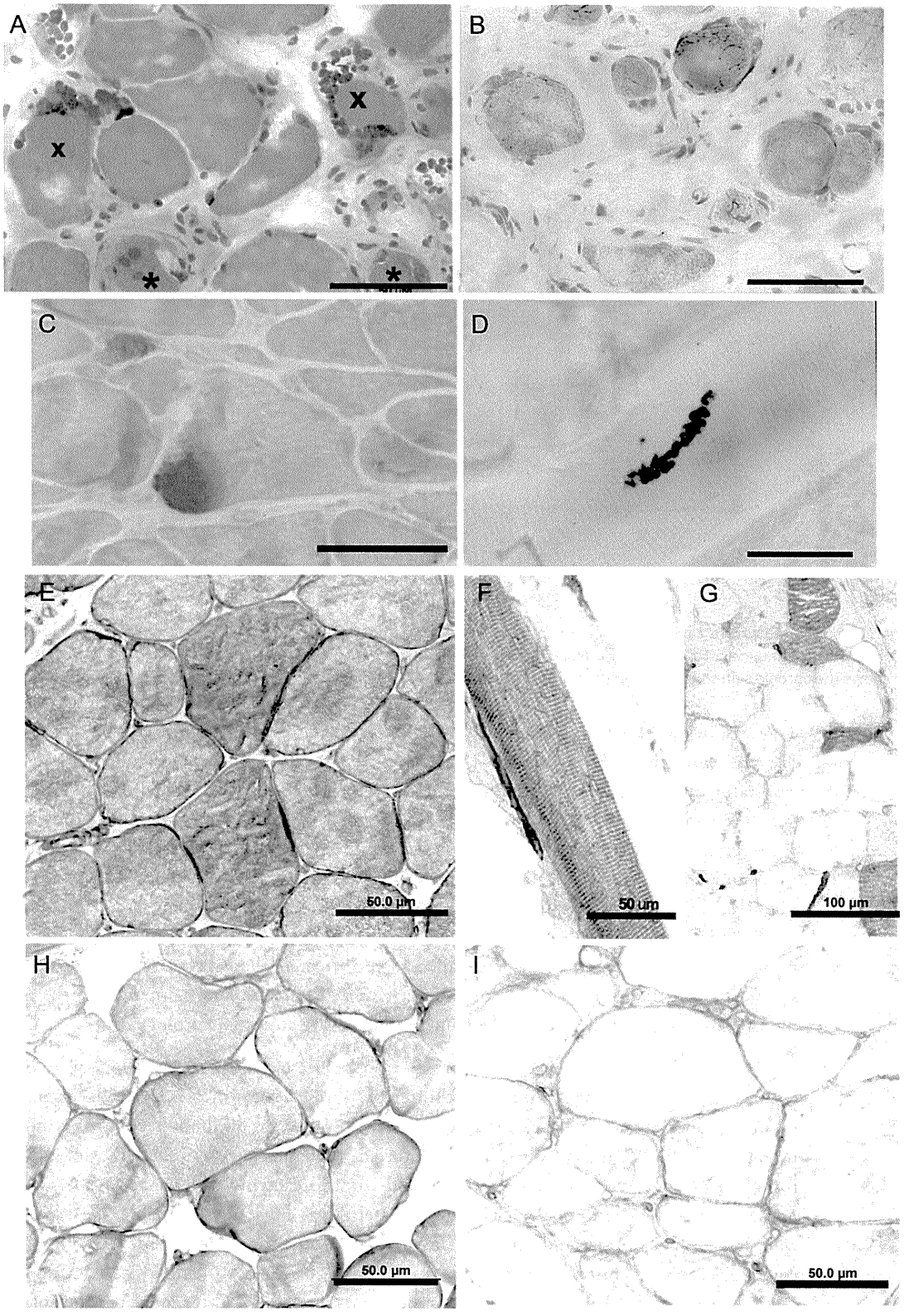

(A, B) Note marked variation in fiber size, regenerating fiber elements (asterisks), endomysial fibrosis (B), and clusters of large nuclei at periphery of several fibers. (C) Alizarin red stain reveals focal calcium deposits in 2 fibers. (D) Multiple small cholinesterase-reactive endplate regions arrayed over an extended length of the fiber. Plectin was localized in normal control muscle (E, H) and patient intercostal muscle (F, G, I) with antibody recognizing the plectin rod domain (anti-Rod Ab) (E–G) and antibody recognizing the C-terminal plectin domain (anti-C Ab) (H, I). (E, H) In normal muscle, plectin is localized to the sarcolemma and sarcoplasm with both Abs. The anti-Rod Ab shows plectin-depleted and plectin-positive muscle fibers (F, G), whereas the anti-C Ab shows sarcoplasmic loss and slight sarcolemmal expression of plectin in all muscle fibers (I). Bars indicate 50 μm in all panels except in (G), where they indicate 100 μm.

Figure 3 **Ultrastructural findings in abnormal muscle fibers of patient 2**

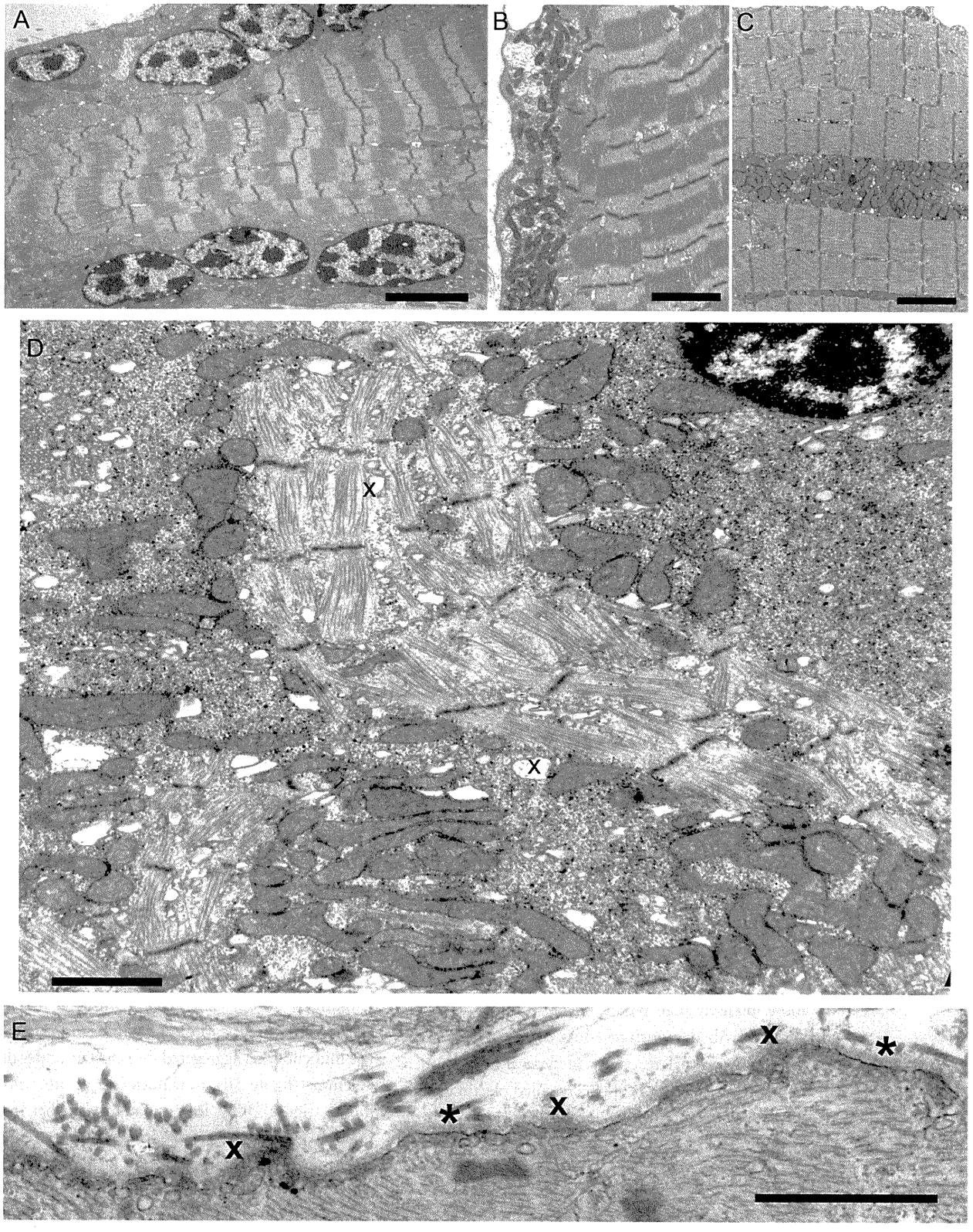

(A) Note subsarcolemmal rows of large nuclei harboring multiple prominent chromatin bodies. (B, C) Subsarcolemmal and intrafiber clusters of mitochondria surrounded by fiber regions devoid of mitochondria. (D) Aberrant and disrupted myofibrils surrounded by clusters of mitochondria intermingled with glycogen, ribosomes, and dilated vesicles (x). Note preapoptotic nucleus at upper right. (E) Focal sarcolemma defects due to gaps in the plasma membrane. Where the plasma membrane is absent, the overlying basal lamina is thickened (x). Small vesicles underlie the thickened basal lamina. Asterisks indicate segments of the preserved plasma membrane. Bars = 4 μm in (A), 3 μm (B, C), 1.4 μm in (D), 1 μm in (E).

Figure 4 **Abnormal endplate (EP) regions in patient 2**

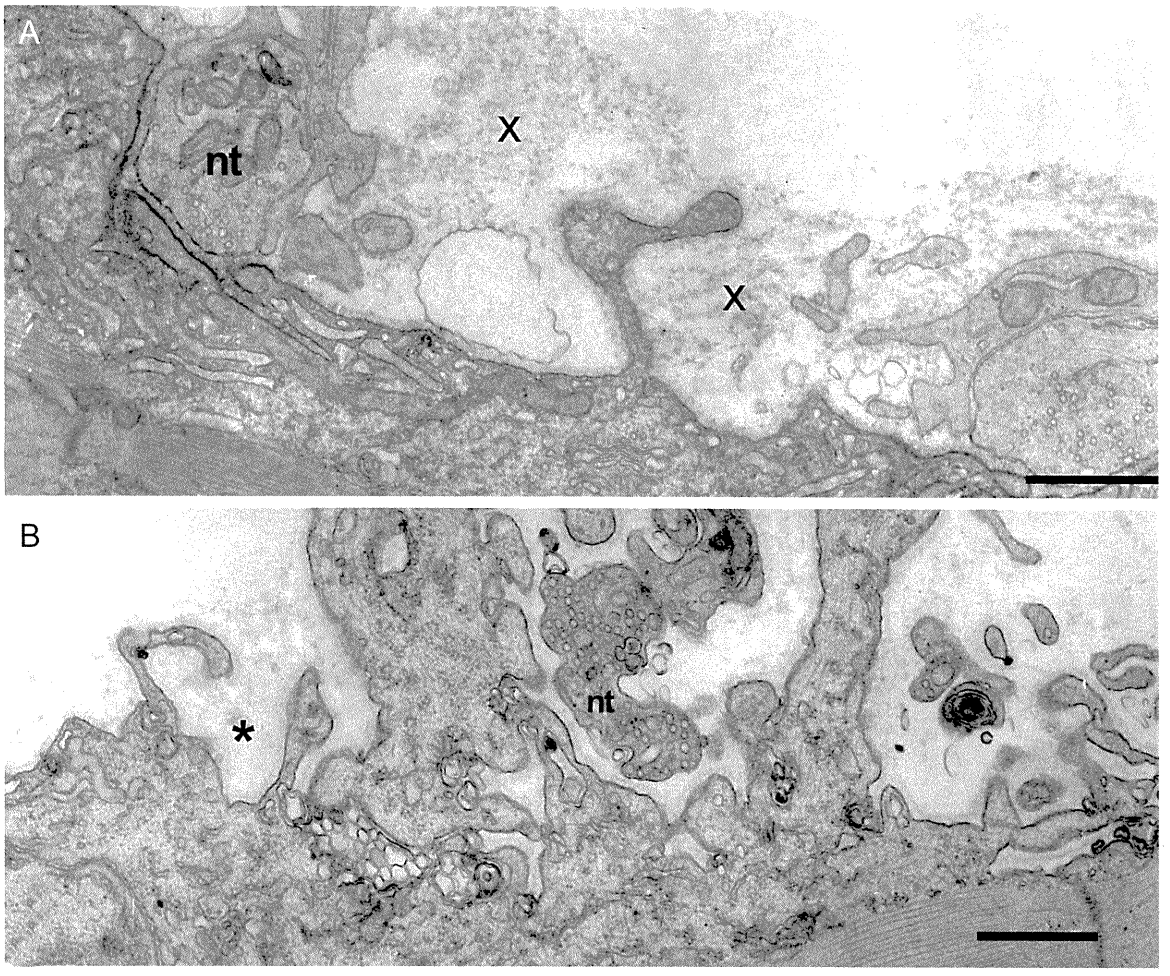

(A) The imaged EP regions show partial occupancy of the postsynaptic region by the nerve terminal and remnants of degenerate folds (x). The nerve terminal (nt) occupies only part of the postsynaptic region. Degenerate remnants of the folds (x) appear over the simplified postsynaptic region from which folds were lost. Dark reaction product on postsynaptic membrane shows acetylcholine receptor localization with peroxidase labeled α-bungarotoxin. (B) Small nerve terminal occupies only part of a highly simplified postsynaptic region. Asterisk indicates remnants of basal lamina that surrounded preexisting folds. Bars = 1 μm.

ated nerve fibers (not shown). In normal muscle, the anti-Rod Ab (figure 2E) was more reactive than the anti-C antibody (figure 2H) and stained type 1 fibers more intensely than type 2 fibers. In the patients, the anti-Rod Ab demonstrated loss of sarcoplasmic and trace sarcolemmal reactivity in type 1 fibers but, as noted by others,[19] type 2 fibers retained plectin positivity (figure 2, F and G, and figure e-2). In contrast, the C-20 Ab revealed no sarcoplasmic and only slight sarcolemmal reactivity in all fibers (figure 2I).

Muscle fiber ultrastructure in P2. ***Nuclear abnormalities.*** Consistent with light microscopy, numerous muscle fibers harbored subsarcolemmal rows or clusters of large ovoid nuclei containing 3 to 10 large, highly electron dense chromatin deposits (figure 3A). Nuclei in other fiber regions were of normal size and heterochromatic or euchromatic. Some nuclei harbored large clumps of heterochromatin with small islands of euchromatin indicating preapoptotic changes (figure 3D).

Mitochondrial abnormalities. In some fibers, the mitochondria were normally aligned with the Z disk and evenly distributed in the muscle fiber. In other fibers, the mitochondria aggregated into clusters under the sarcolemma (figure 3B), near nuclei, or in other fiber regions (figure 3C), leaving adjacent fiber regions depleted of mitochondria. Some mitochondrial aggregates were interspersed with glycogen granules, ribosomes, and dilated vesicles (figure 3D).

Myofibrillar abnormalities. Aberrant myofibrils appeared among dislocated organelles in both atrophic and nonatrophic fibers (figure 3D). Disintegration and streaming of Z disks were detected in some fiber regions with or without myofibrillar disarray. A few abnormal fiber regions harbored small nemaline rods. End-stage muscle fibers contained few mitochondria, remnants of

Figure 5 **Plectin domains and identified *PLEC* variants**

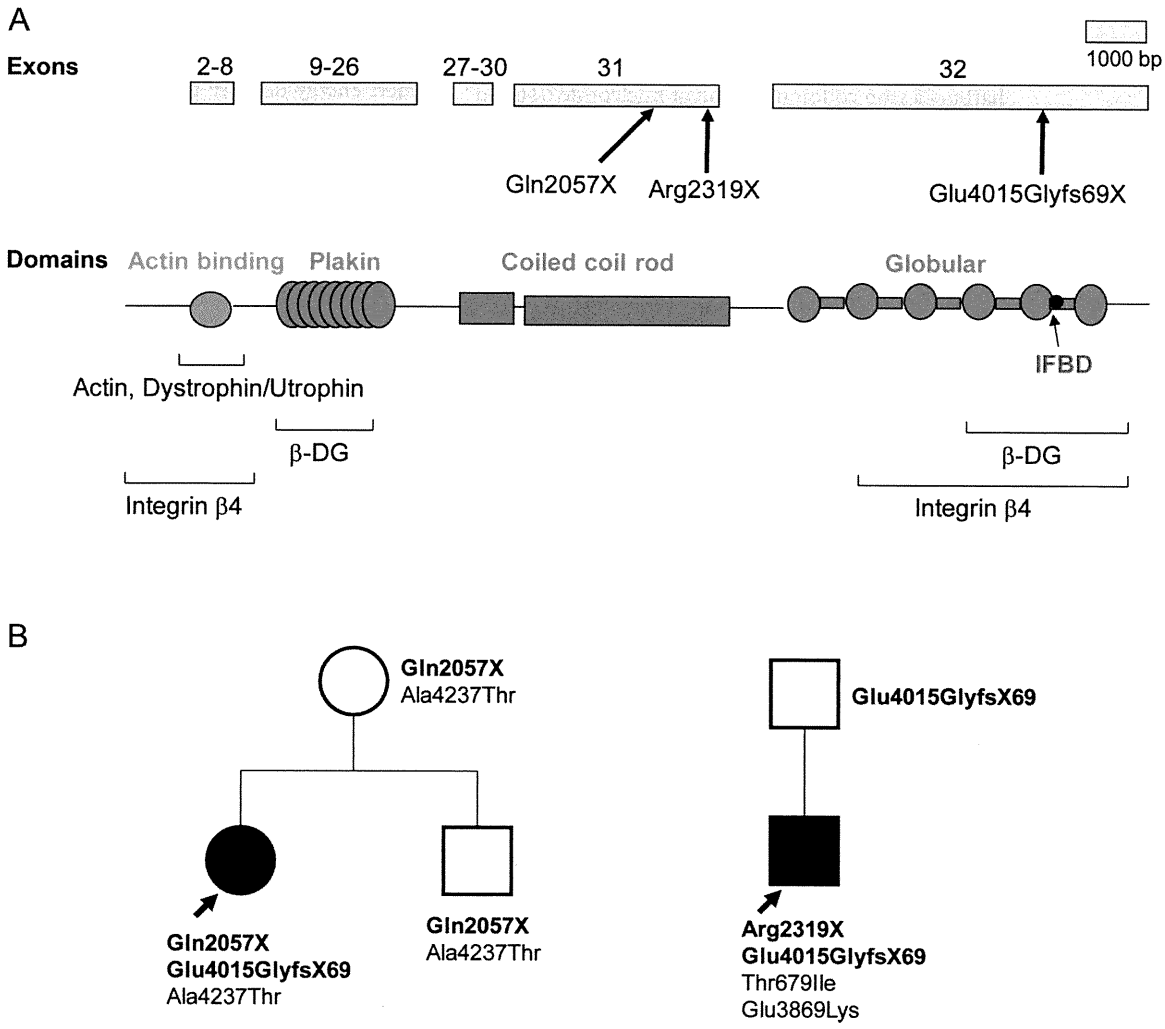

(A) Schematic representation of *PLEC* exons 2–32 indicating identified patient mutations and binding domains associated with C- and N-terminal regions of plectin.[39] (B) Family analysis of P1 and P2 shows transmission of pathogenic mutations (bold face) and polymorphisms.

Z disks with attached short filaments (Z brushes), and debris. Small membrane-bound vacuoles of different sizes that likely represent dilated components of the sarcoplasmic reticulum appeared in fiber regions with or without other abnormalities (figure 3D).

Sarcolemmal defects. The focal subsarcolemmal calcium deposits in scattered muscle fibers prompted us to search for sarcolemmal defects at the ultrastructural level and we detected these in some fibers of both patients. Where the plasma membrane was discontinuous, it was often covered by focally thickened basal lamina (figure 3E).

Endplate studies in P2. Synaptic contacts on the muscle fibers, visualized by the cholinesterase reaction, consisted of multiple small EP regions arrayed over an extended length of the muscle fiber (figure 2D). This finding has been observed in other patients with ongoing destruction and remodeling of the postsynaptic region.[31]

Colocalization of plectin and AChR by fluorescence microscopy showed strong expressions of plectin and AChR at normal EPs. At patient EPs AChR expression was not appreciably attenuated but plectin expression was barely perceptible (figure e-3).

On electron microscopy, some EP regions appeared normal but many had an abnormal conformation, displaying one or more of the following: partial occupancy of the postsynaptic region by nerve terminals, small nerve terminals, atrophic and remnants of degenerated junctional folds resulting in highly simplified postsynaptic regions, and nerve sprouts near degenerating EPs (figure 4 and figure e-4). Table e-1 shows the frequency of the observed conformational changes. Table e-2 shows morphometry revealing reduced size of presynaptic and postsynaptic EP components.

Genetic analysis. Genetic analysis was challenging owing to the very large size of the *PLEC* transcript

(~14 Kb vs ~11 Kb for dystrophin), the very large exons 31 (3381 bp) and 32 (6219 bp), multiple splice variants of exon 1, and polymorphisms that may be race-dependent. Eventually we detected 2 truncating mutations in each patient (figure 5). P1 harbors a stop codon mutation at nucleotide 6169 in exon 31 (c.6169C>T/p.Gln2057X), and a duplication at nucleotide 12043 in exon 32 that predicts 68 missense codons followed by a stop codon (c.12043dupG/p.Glu4015GlyfsX69). P2 harbors a previously reported nonsense mutation at nucleotide 6955 in exon 31 which generates a stop codon (c.6955C>T/p.Arg2319X),[16] and the same duplication mutation detected in P1 (figure 5B). Presence of the pathogenic mutation was confirmed at the cDNA level in both patients. Both stop codon mutations abrogate, and the c.12043dupG mutation disrupts, the IF binding site and one of the two β-dystroglycan and integrin β4 binding sites (figure 5A).

Both patients also harbored polymorphisms not listed in the SNP database (see figure 5B). In P1, p.Ala4237Thr was deemed a polymorphism because it appeared together with Gln2057X in the unaffected mother. In P2, p.Thr679Ile was present in 1 of 60 African Americans and p.Glu3869Lys in 1 of 100 African Americans, although both variants were absent in 200 Caucasians.

It has been suggested that expression of the rodless plectin transcript may mitigate the plectinopathy phenotype.[32] We therefore confirmed presence of the rodless domain by sequencing cDNA and used real-time PCR to compare the relative abundance of the rodless transcript in P1, P2, and 3 normal controls. The rodless transcript/full transcript ratio was 0.15 in P1, 0.32 in P2, and 0.22 ± 0.03 (mean ± SD) in 3 controls.

DISCUSSION Although each patient carries a nonsense mutation in *PLEC* exon 31 and an identical frameshift mutation in exon 32, the tempo of the disease was faster in P2 than in P1. In P2, EBS presented at age 6 weeks, MyS at age 3 years, and he lost ambulation by age 18 years. In P1, MyS presented at age 9 years, EBS at age 18 years, and she can still take a few steps at age 31 years. It has been suggested that expression of the rodless transcript can mitigate the phenotype in patients who carry mutations in the plectin rod domain.[32] However, real-time PCR indicates that expression of the rodless transcript was higher in the more severely affected P2. Thus in the patients studied by us the abundance of the rodless transcript was not a reliable indicator of the clinical phenotype.

Dislocation of the fiber organelles apparent at the ultrastructural level has multiple predictable consequences. Abnormal alignment and displacement of the myofibrils weakens or eliminates their contractile strength; separation of mitochondria from myofibrils renders energy delivery to contracting myofibrils inefficient. The eccentrically positioned large nuclei with multiple chromatin deposits may be dysfunctional or inefficient in their translational activities and in nuclear-cytoplasmic trafficking when not adjacent to organelles or fiber domains they subserve. Injury to the inadequately supported plasma membrane is evidenced by subsarcolemmal calcium deposits and sarcolemmal defects in a proportion of the fibers (see figure 2C, figure 3E, and figure e-1). Most of these were smaller than those in Duchenne dystrophy[27,33] but they still likely contribute to fiber injury and, if large, they may contribute to fiber necrosis.

Electron microscopy of the EPs indicates that plectin deficiency targets the junctional folds for destruction. When sarcomeres contract and relax, the extrajunctional sarcolemma bulges and relaxes but the junctional folds maintain a constant architecture.[34] This mandates enhanced rigidity of the junctional folds and renders them especially vulnerable to mechanical stress. Thus loss of cytoskeletal support of the junctional folds due to the plectin deficiency, as depicted in figure e-3, readily explains the progressive destruction of the folds. Destruction of junctional folds decreases the density or eliminates the voltage-gated Na^+ channels which are concentrated in troughs between the folds[35,36] and this increases the threshold for action potential generation.[37] Destruction of the folds also decreases the input resistance of the postsynaptic membrane and thereby the amplitude of synaptic potential.[38] Widening of the synaptic space reduces the concentration of acetylcholine before it reaches the junctional folds. The combination of these factors decreases quantal efficacy and compromises the safety margin of neuromuscular transmission. The relentless progression of the myasthenic symptoms in both patients implies that formation of new EP regions eventually fails to compensate for the ongoing destructive changes.

Why only a proportion of the muscle fibers is affected in a given muscle, and why some EPs are more severely affected than others, remain unanswered questions. It is uncertain that it can be attributed to preserved plectin expression in type 2 fibers, as shown by the 10F6 anti-Rod antibody. First, the anti-C terminal antibody showed nearly complete plectin deficiency in all muscle fibers in both patients. Second, the anti-rod domain antibody showed either no plectin reactivity in any fiber, or preserved immunoreactivity in type 1 instead of type 2 fibers.[19]